A Continuous-Effect Membrane Distillation Process Based on Hollow Fiber AGMD Module with Internal Latent-Heat Recovery

Kun Yao, Yingjie Qin, and Yingjin Yuan
School of Chemical Engineering and Technology, Tianjin University, Tianjin 300072, P.R. China

Liqiang Liu, Fei He, and Yin Wu
Chembrane Research and Engineering, Inc., Bridgewater, NJ 08807

DOI 10.1002/aic.13892
Published online September 13, 2012 in Wiley Online Library (wileyonlinelibrary.com).

A continuous-effect membrane distillation (CEMD) process was developed by equipping air gap membrane distillation (AGMD)-based and strictly-parallel hollow fiber module with internal heat recovery. Its performance was indicated by flux, performance ratio and evaporation efficiency. Two kinds of CEMD modules made from different membrane fibers were tested. A face-centered central composite experimental design was conducted to investigate the influences of operating variables including cold-feed temperature, hot-feed temperature, and feed-in flow rate on the performance. Within the studied experimental range, the maximum PR of 13.8 was obtained. A theoretical model based on governing transport equations was established to predict the process performance, and the model described the experimental data fairly well. In light of the model, possible ways to further increase PR were predicted. The dilute aqueous sugar solution was successfully concentrated 12-fold to a final concentration of about 20 wt % by using CEMD process with a final PR of 8.2. © 2012 American Institute of Chemical Engineers *AIChE J,* 59: 1278–1297, 2013
Keywords: continuous-effect membrane distillation, air gap membrane distillation, hollow fiber module, internal heat recovery, performance ratio

Introduction

Membrane distillation (MD) is a hybrid of thermal distillation and membrane process in which evaporation of volatile species (e.g., water) takes place at the interface between aqueous feed solution and a hydrophobic microporous membrane, and then vapors can pass through the micropores to the other side of the membrane (permeate side) by convective or diffusive mechanism. The driving force for mass transport of vapors is the difference in partial vapor pressure. According to various operation modes employed on the permeate side to impose the pressure difference, MD process can be divided into direct contact membrane distillation (DCMD), air-gap membrane distillation (AGMD), vacuum membrane distillation (VMD), sweeping gas membrane distillation (SGMD), and osmotic distillation (OD). Detailed and extensive reviews on MD have been provided by Lawson and Lloyd,[1] Curcio and Drioli,[2] and Khayet et al.[3]

A large amount of work has been performed in the last 25 years with regard to the aforementioned MD configurations. Nonetheless, from a commercial standpoint, MD cannot yet compete with the conventional multistage flash (MSF), multiple effect distillation (MED), and reverses osmosis (RO) despite its advantages, and is still not implemented at industrial scale for separation of water from aqueous solutions containing nonvolatile solutes. One of the biggest barriers in the industrialization of MD process is the high-thermal energy consumption required for evaporation, which represents a large fraction of operation expenses. The thermal energy efficiency of an evaporation-based separation process such as MSF, MED and MD is commonly measured as ''performance ratio'' (PR), whose definition is the quotient of the amount of latent heat needed for evaporation of the produced water and the amount of heat provided to the system from an external energy source. A typical *PR* of MED for desalination is about 8.0–16.0.[4] Unfortunately, the value of *PR* for any traditional MD process (no heat recovery/recycle is employed) reported in literature is typically less than 1.0.

In the most studied DCMD process, *PR* generally ranged from 0.1–0.65 which varied with the membrane used.[5–7] Under the same feed condition, higher vapor permeation and *PR* were achieved for VMD when compared to DCMD.[8] However, a drawback of VMD is that the permeate vapor collection demands evacuation and high-condenser capacity. Moreover, membrane wetting or leakage is also a grievous problem due to large transmembrane pressure difference. Because of low-thermal conductivity of the air gap, AGMD can prevent the conduction losses greatly and, is, thus, with a relatively high *PR* of 0.70–0.98,[9,10] but the introduction of the air gap and the extra cooling-wall increases the

Correspondence concerning this article should be addressed to Y. Qin at yjqin@tju.edu.cn.

constructional complexity of the module and also the mass-transfer resistance, which leads to generally lower flux than that of DCMD under the same driving force.[11] Unlike in DCMD and VMD processes, hollow fiber modules are rarely reported for AGMD process. The concept of strictly parallel multiple hollow fibers-based AGMD process was first theoretically modeled by Chen et al.[12]

Triggered by recovery of the latent heat of condensation in MSF and MED processes, heat recovery was also proposed for MD process,[13,14] where the latent heat released during condensation was used to preheat the cold feed. Thus, only a small amount of heat is needed to be supplied externally for the following evaporation. It is believed that the realization of heat recovery in a MD process should be an essential way to compete commercially with MSF, MED and RO processes.

There are two strategies available to recover the latent heat of condensation, i.e., external heat recovery and internal heat recovery. External heat recovery was usually realized by integrating DCMD with external heat exchangers. A diagram for a hollow fiber-based DCMD module with an external heat exchanger was first illustrated by Fane et al.[15] Kurokawa and Sawa[16] further found that the optimal *PR* in their plate membrane-based DCMD system with heat recovery unit was about 3.0. Gilron et al.[17] pointed out that the highest *PR* for a standalone cross-flow DCMD module with external heat recovery would be no more than 2.2, and also predicted that *PR* could potentially reach as high as 12.0 by combining these modules into a countercurrent cascade as a single block. Lee et al.[18] further carried out experiments by using cascades consisting of 2–8 DCMD stages in conjunction with heat exchangers. The highest reported experimental value of *PR* was between 5.0 and 6.0.

Internal heat recovery was realized by inserting a heat recovery unit within a single MD module. There exists an interior condensation surface originally in an AGMD module, thus, it naturally equips AGMD module with the function of internal latent-heat-recovery. The first AGMD module in a "sandwich" embodiment with internal heat recovery was patented by Henderyckxa in 1971.[19] Gore et al.[20] provided a spirally wound AGMD module with flat membranes, and the *PR* could reach as high as 11.0 for desalination. Koschikowski et al.[21] have also reported the value of PR ranged from 3.0–6.0 when a similar spiral wound module which was thermally driven by solar energy was used.

Compared to flat membrane-based modules, hollow fiber-based AGMD modules with internal heat recovery are preferable due to their high-specific surface area. As early as in 1999, Guijt et al.[22] presented a schematic of countercurrent flow transmembrane evaporation module, which consisted of several vertical membrane fibers with a cooling plate parallel placed on both sides separated by air gap. Guijt et al.[23] also carried out experiments by using a cylindrical module constructed in the form of two concentric fibers with a well-defined annular air gap. Hanemaaijer et al.[24] patented one AGMD embodiment to yield macroscopically countercurrent flow pattern by connecting a number of cross-flow module segments together, each of that was equipped with hollow fibers arrays for both the feed and retentate stream. Furthermore, the Memstil® process was developed which claimed that the *PR* for desalination was in the range of 9–29.[25]

The aforementioned MD processes based on hollow fiber modules by either external[18] or internal[24] heat recovery show the characteristics of multiple-effect operation; therefore, the concept of multiple effect membrane distillation (MEMD) is introduced as a term to describe the MD processes in an operation mode of separate stages/effects with a *PR* much more than 1.0. The objective of this study is to develop a new kind of process also achieving a *PR* much more than 1.0, which is based on the use of hollow fibers-based AGMD module, and is operated in a strictly countercurrent mode, capable of internal heat recovery. Such a process has two distinct characteristics: (1) the evaporator tubing (usually porous hydrophobic hollow fiber) is exactly in parallel with the condenser tubing (nonporous hollow fiber) so that the cold-feed and the hot-feed are strictly countercurrent, and, thus, the condensation heat is recovered at maximum; (2) unlike the discrete segments or cascades in MEMD configurations, this simple once-through module in reality has a continuum of stages/effects to achieve a high *PR* value. Thus, to show its distinctiveness, this process is, hereafter, called as continuous-effect membrane distillation (CEMD). In this article, the experimental results are presented for the performance evaluation of CEMD modules made from different hollow fibers. Empirical and theoretical models were also built to describe performance-operation relations.

In cellulosic ethanol production, to resolve the contradiction between the sugar concentration obtained in enzymatic hydrolysis and that required for the following fermentation, it is necessary to add a preconcentration unit between the two steps. Zacchi and Axelsson[26] found that the cost of preconcentration using a six-effect evaporator was still high, mainly for expensive steam provided. In this article, the CEMD process with a much higher *PR* value than the six-effect evaporator also with a low-grade heat source was applied to concentrate the dilute aqueous sugar solution 12 times.

Continuous-Effect Membrane Distillation Technique

Description of CEMD process via MSF

As a comparison, MSF process is briefly described. Figure 1a shows the typical schematic of a conventional once-through MSF unit, which consists of several consecutive stages maintained at decreasing pressure. In each stage, flashing occurs and the flashed vapor is condensed as distillate on the outside surface of the condenser tubing where the feed stream flows. Thus, the feed is gradually heated by the condensation vapor heat. The necessary heat input to the feed stream is provided by an external heat exchanger. Vacuum is usually required in MSF processes.

The configuration of the CEMD process is presented in Figure 1b, which includes an AGMD module consisting of strictly parallel evaporator fiber and condenser fiber with internal heat-exchanging function (thus, also called as CEMD module), and an external heat exchanger. The cold feed stream flows into the lumen side of nonpermeable hollow fiber (thereafter called *dense-wall fiber*), whereby it is gradually warmed-up by condensation of the vapor on its outside surface, then leaves the dense-wall fibers and enters into an external heat exchanger to be further heated-up to a higher temperature. Then the hotter feed goes back counter-currently into the lumen side of hydrophobic porous permeable hollow fiber (thereafter called *porous fiber*), where the feed evaporates and the vapor diffuses across the porous wall, and then the air gap to the outside surface of dense-wall

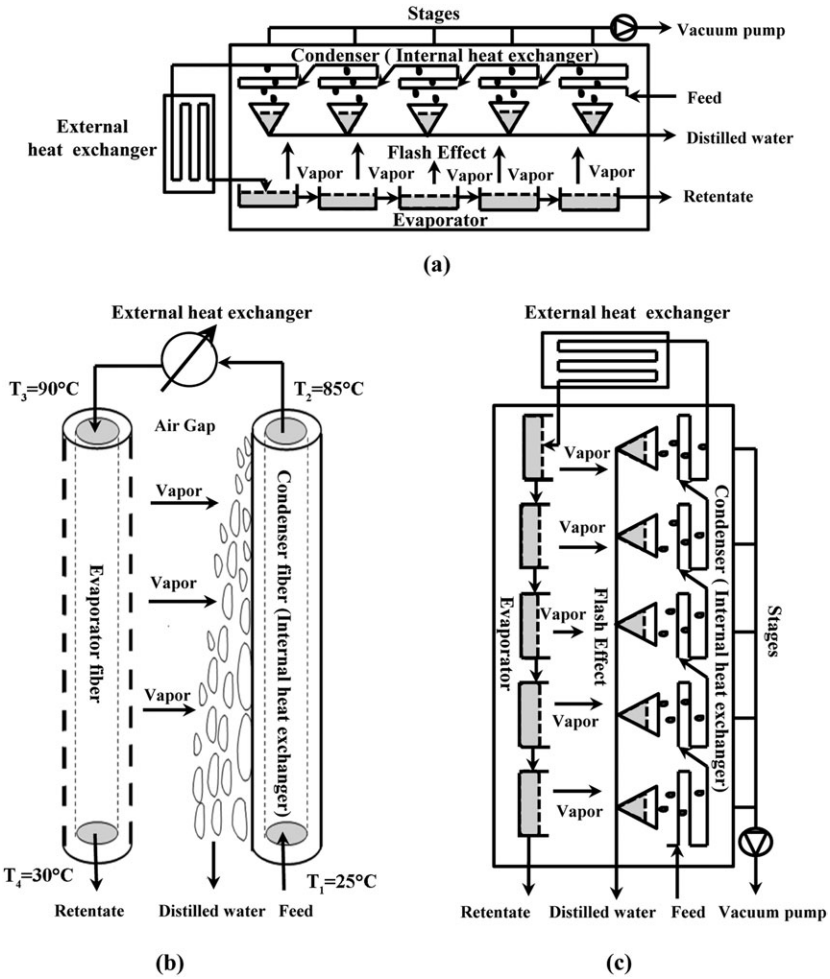

Figure 1. Schematic plots of (a) a conventional MSF unit and comparison between, (b) CEMD process, and (c) MSF unit rotated by 90°.

fiber, on which the vapor condenses while releasing the latent heat to the adjacent cold feed stream. Driven by gravitation, the condensed distillate film flows down in countercurrent with the cold feed, which further leads to the recovery of the perceptible heat of the distillate. Thus, the cold feed becomes hot at the outlet of the dense-wall fiber. The CEMD process is similar to that of once-through MSF process rotated by 90° (see Figure 1c). The configuration of CEMD is the miniature of MSF, and combines the advantages of both MD and MSF into one compact membrane module with an external heat exchanger. When such a process is used for separation, boiling, entrainment will not happen and vacuum is not necessarily required as the porous hydrophobic membrane is used as the evaporator.

The details of the aforementioned CEMD module are illustrated in Figure 2a. Two sets of different hollow fibers, i.e., dense-wall fibers and porous fibers are mixed well and closely packed in parallel together inside a cylindrical shell. In such an assembly, the space between the adjacent fibers is filled with air. At each end, the fibers are split into two separate bundles, each containing porous fibers or dense-wall fibers, respectively, which are taken out through two exits at each end of the shell, and potted with epoxy. Near the bottom of the shell side, there is an exit as the distillate outlet. Ideally, the bundle of fibers should be arranged in a way that a porous fiber is immediately adjacent to a dense-wall fiber, and, thus, a porous fiber is only surrounded by dense-wall fibers and a dense-wall fiber is surrounded by porous fibers.

Overall balances and calculation of performance indicators

Figure 2b shows a schematic diagram of all flows entering and leaving CEMD module operated with countercurrent pattern. At the macroscopic level, the following equation can be derived on the basis of overall energy and mass balances

$$\mathrm{W_F} \cdot H_3 + \mathrm{W}_F \cdot H_1 = W_F \cdot \mathrm{H}_2 + W_D \cdot H_D + (W_F - W_D) \cdot H_4 + Q_{\mathrm{loss}} \quad (1)$$

where W_F and W_D (kg/h) are the mass flow rates of feed-in stream and distillate, respectively; H_1, H_2, H_3, H_4 and H_D (J/kg) are the stream enthalpies at the inlet of dense-wall fibers, outlet of dense-wall fibers, inlet of porous fibers, outlet of porous fibers and outlet of distillate, respectively; Q_{loss} (J/h) is the external heat loss from the module to the surrounding.

Assuming the specific heat capacity $C_{p,l}$ (J/kg·°C), and density ρ (kg/L) of the process stream (feed-in, feed-out and distillate) are the same and constant when the feed is simply

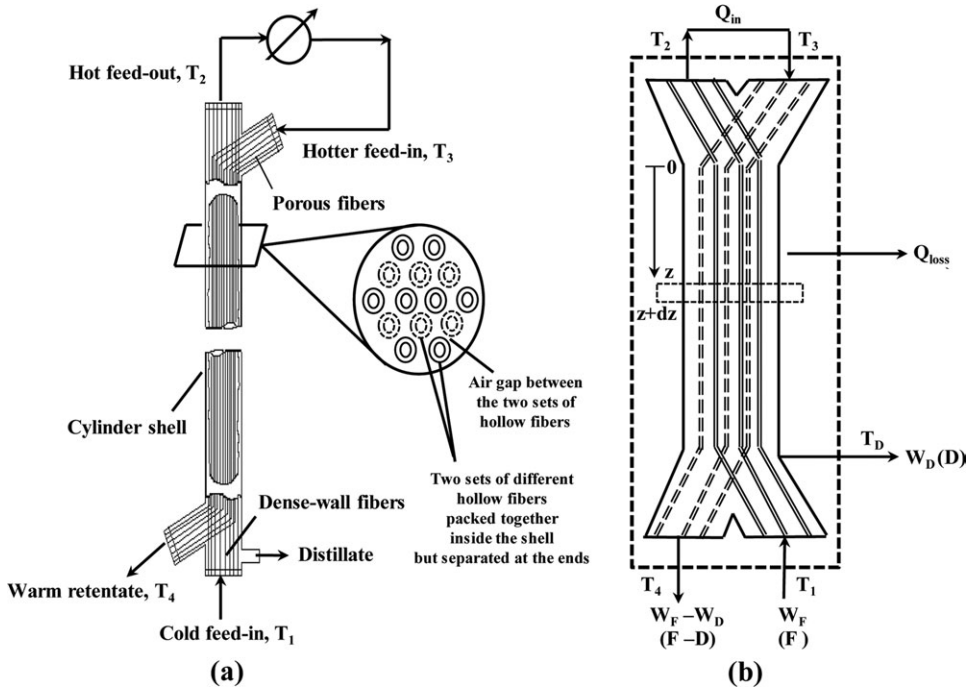

Figure 2. (a) Configuration of CEMD module, and (b) schematic diagram of all flows entering and leaving CEMD module with countercurrent pattern.

pure water or very dilute aqueous solution, Eq. 1 can be rewritten as

$$W_F \cdot (H_3 - H_2) + W_D \cdot (H_4 - H_D) - Q_{\text{loss}} = W_F \cdot (H_4 - H_1) \tag{2}$$

$$\rho \cdot F \cdot C_{p,l} \cdot (T_3 - T_2) + \rho \cdot D \cdot C_{p,l} \cdot (T_4 - T_D) - Q_{\text{loss}} = \rho \cdot F \cdot C_{p,l} \cdot (T_4 - T_1) \tag{3}$$

or

$$\frac{T_3 - T_2}{T_4 - T_1} + \frac{D \cdot (T_4 - T_D)}{F \cdot (T_4 - T_1)} - \frac{Q_{\text{loss}}}{\rho F C_{p,l}(T_4 - T_1)} = 1 \tag{4}$$

where F and D (L/h) are the volumetric flow rates of feed-in and distillate, respectively; T_1, T_2, T_3, T_4 and T_D (°C) are the stream temperatures at the inlet of dense-wall fibers, outlet of dense-wall fibers, inlet of porous fibers, outlet of porous fibers and outlet of distillate, respectively.

When the CEMD module is ideally insulated and the heat loss to the surrounding can be neglected, the third term on the left side of Eq. 4 becomes zero. The value of T_D, which is certainly between T_1 and T_4, is usually more close to T_1. In a typical operation of CEMD process, the ratio between D and F, which is defined as fractional recovery, $R = D/F$, is usually less than 9%. The second term on the left side of Eq. 4 is thus certainly less than 9%; the first term on the left side of Eq. 4 would be

$$0.91 < \frac{\Delta T_{\text{top}}}{\Delta T_{\text{bottom}}} = \frac{T_3 - T_2}{T_4 - T_1} < 1 \tag{5}$$

where ΔT_{top} and ΔT_{bottom} are the horizontal temperature differences at the top and the bottom of the module, respectively.

If the heat loss to the surrounding cannot be negligible, there will be $\Delta T_{\text{top}} \leq \Delta T_{\text{bottom}}$ for small heat loss, and $\Delta T_{\text{top}} > \Delta T_{\text{bottom}}$ for large loss.

In a CEMD process, distillate flux, PR and evaporation efficiency are the most important performance indicators for process evaluation.

The distillate flux is calculated by

$$J_D = D/S_{pi} \tag{6}$$

where J_D is the volumetric distillate flux (L/m^2·h), and S_{pi} is the effective evaporation surface area based on inner diameter of the porous fiber.

The necessary heat input provided from the external heat source via a heat exchanger to CEMD module, Q_{in}, can be calculated by

$$Q_{in} = W_F \cdot C_{p,l} \cdot (T_3 - T_2) = \rho F C_{p,l}(T_3 - T_2) \tag{7}$$

Thus, PR can be written as

$$PR = \frac{W_D \cdot \Delta H_v}{Q_{in}} = \frac{D \cdot \Delta H_v}{F \cdot C_{p,l} \cdot (T_3 - T_2)} = \frac{R \cdot \Delta H_v}{C_{p,l} \cdot (T_3 - T_2)} \tag{8}$$

where ΔH_v (J/kg) is the evaporation heat of feed stream, which is a function of temperature and feed composition. ΔH_v can be well thought of as the evaporation heat of pure water in this study, and is expressed as follows[22]

$$\Delta H_v = 2.2452 \cdot 10^6 + 2475(373.0 - (T(^{\circ}C) + 273.15)) \tag{9}$$

The evaporation efficiency η, which is defined as the percent of heat transferred in the form of mass, i.e.,

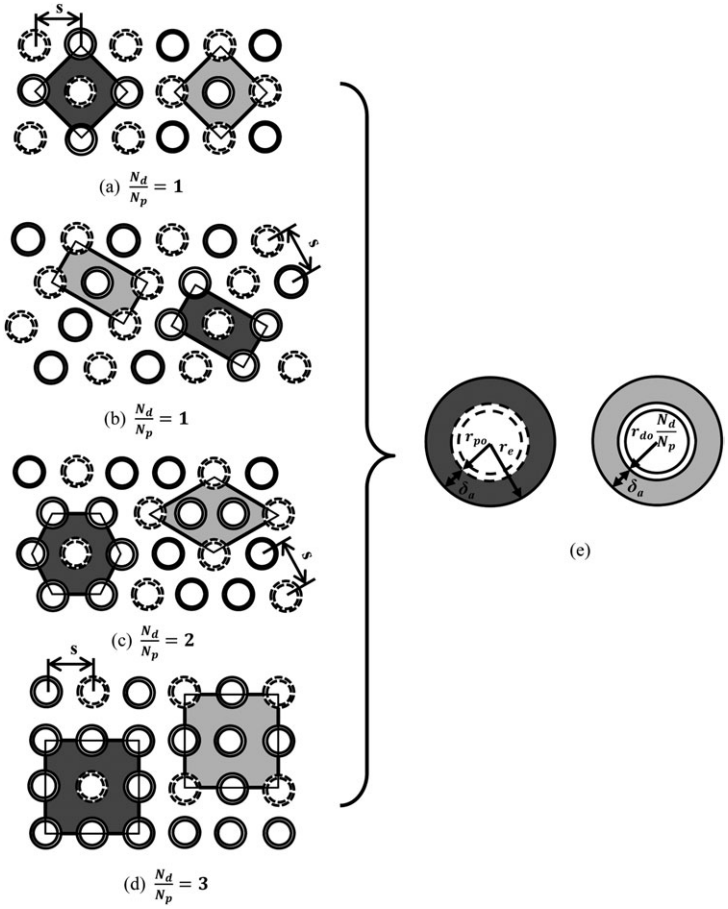

Figure 3. Possible ideal packing arrangements in the cross section of fiber populations and its hypothetical cell unit.

evaporation-condensation, in the total heat transferred from the hot feed. Referring to Eqs. 1 and 3, η could be expressed as

$$\eta = \frac{W_D \cdot \Delta H_v}{W_F \cdot H_3 - (W_F - W_D) \cdot H_4 - W_D \cdot H_D} = \frac{W_D \cdot \Delta H_v}{W_F \cdot H_2 - W_F \cdot H_1 + Q_{\text{loss}}} = \frac{D \cdot \Delta H_v}{F \cdot C_{p,l} \cdot (T_2 - T_1) + Q_{\text{loss}}/\rho} \tag{10}$$

When Q_{loss} is negligible

$$\eta = \frac{D \cdot \Delta H_v}{F \cdot C_{p,l}(T_2 - T_1)} = \frac{R \cdot \Delta H_v}{C_{p,l}(T_2 - T_1)} \tag{11}$$

PR and η are two indicators for efficiency of thermal energy utilization, which, respectively, tell how much energy is recovered by internal latent-heat-recovery and how much energy is lost due to internal heat loss (conduction). For ordinary membrane distillation such as AGMD, DCMD and VMD without heat recovery, the value of *PR* is equivalent to that of η and less than 1.0.

Theoretical Approach

Basic assumptions

When it is tried to model CEMD process, some assumptions are necessary. First it is assumed that the packed hollow fibers are parallel, distributed uniformly within the shell. Cylindrical hollow fibers could be ideally packed together in a square or triangular arrangement.[27] Schematics of possible ideal packing arrangements for different number ratio of dense-wall fibers to porous fibers (N_d/N_p) in the cross section are shown in Figure 3a–d, and *s* is the distance between the centers of two adjacent fibers (same or different kind). Figure 3a and 3d indicate the square arrangements when $N_d/Np = 1$ and $N_d/Np = 3$. Figure 3b and 3c indicate the triangular arrangements when $N_d/Np = 1$ and $N_d/Np = 2$. As shown in each arrangement, both heat and mass are transported through the air gap which is plotted in a darkly shaded part from any one porous fiber located in its center to the adjacent dense-wall fibers, and also both heat and mass from the adjacent porous fibers are transported through the air gap which is plotted in a lightly shaded part to any one, two or three dense-wall fibers located in its center. If the boundary effect near the shell is further ignored due to large fiber population, the entire cross section could be divided into a series of unit square, rectangle, hexagon, or rhomboid as shown in Figure 3a–3d. No heat and mass exchange will take place between one such unit, and the other contiguous units due to symmetry. Considering a hypothetical circle embracing one porous fiber, the air gap (darkly shaded part) exists as the annular space created by the hypothetical circle (with the radius of r_e), and the outside surface of porous fiber (with the radius of r_{po}), and so is the dense-wall fiber but with the hypothetical outside radius of $r_{do}N_d/N_p$ to obtain equal air gap

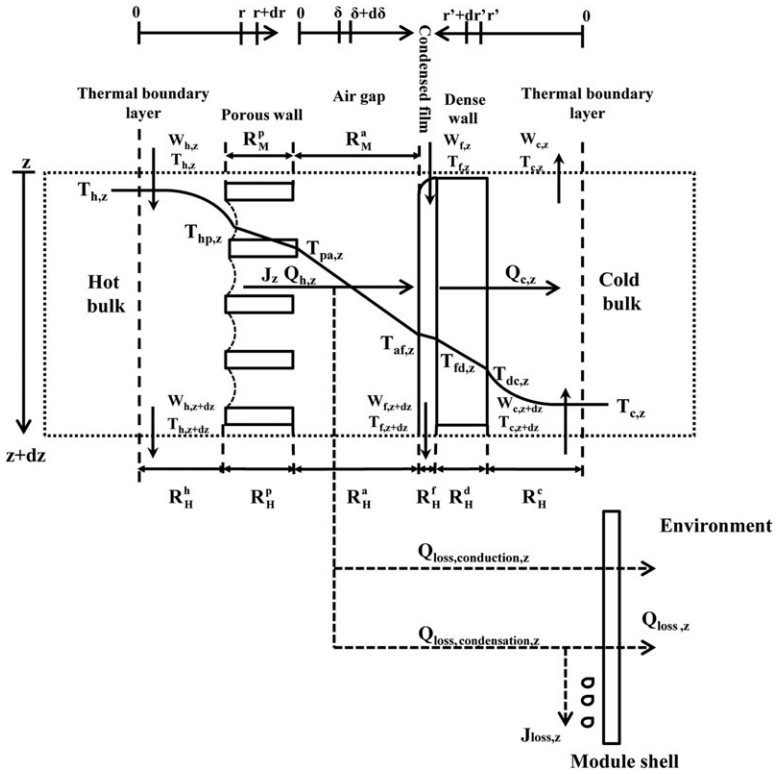

Figure 4. Heat and mass transfer over a differential volume with a length of *dz* in one unit cell basis.

area (the lightly shaded part), as shown in Figure 3e. Thus, the equivalent air gap thickness δ_a, is defined as

$$\delta_a = r_e - r_{po} \tag{12}$$

Then the overall fiber populations could be modeled simply on one unit cell basis, which includes one porous fiber with the outside radius of r_{po}, one dense-wall fiber with the hypothetical outside radius of $r_{do}N_d/N_p$, and the hypothetical air gap of δ_a. There are N_p unit cells in total.

Majumdar et al.[28] gave the detailed geometrical method to estimate δ_a by considering the volume of the air gap, which mainly depends on s, r_{po} and r_{do}. This method was successfully applied in other membrane processes.[29,30] Noted that this equivalent thickness was used based on the outer diameter of porous fiber.

In view of the unit cell given in Figure 3e, the following assumptions are also employed:

1. Operation is carried out under steady state.
2. Heat exchange between shell side and surrounding is assumed to be zero.
3. An ideal plug flow model can be used for feed stream in the lumen side of both fibers.
4. There is no concentration polarization in the lumen side of porous fibers, which is nearly true when the feed is pure water or dilute aqueous solution, fiber with small lumen-side diameter is used, and the distillate flux is relatively small.
5. The vapor remains in phase equilibrium with the liquid at each vapor-liquid interface.
6. The mechanism of mass transfer across the air gap is due to molecular diffusion of vapor through stagnant air.[9,10,12,22,31]
7. The thickness of falling distillate film can be neglected when compared with the air gap or the diameter of dense-wall fibers.
8. An effective air gap thickness δ_a, is assumed to exist along the module length (axial direction) as well as at all radial locations in the fiber bundle.
9. The end effects inside the module are negligible.
10. The deformation of hollow fibers is negligible.

Governing differential equations

The governing equations which are established by heat and mass balances over a differential volume with a length of dz, as depicted in Figure 2b, are summarized later. All heat and mass flows involved in this differential volume are indicated in Figure 4.

Equations for hot feed in the porous fiber lumen, for falling distillate film and for cold flow in the dense-wall fiber lumen are

$$\frac{dW_h}{dz} = -\rho J \cdot N_p \cdot 2\pi r_{pi} \tag{13}$$

$$C_{p,l}\frac{d(W_h T_h)}{dz} = -\frac{dQ_h}{dz} = -q_h \cdot N_p \cdot 2\pi r_{pi} \tag{14}$$

$$\frac{dW_f}{dz} = \rho J \cdot N_p \cdot 2\pi r_{pi} \tag{15}$$

$$C_{p,l}\frac{d(W_f T_f)}{dz} = \frac{d(Q_h - Q_c)}{dz} = (q_h - q_c) \cdot N_p \cdot 2\pi r_{pi} \tag{16}$$

$$\frac{dW_c}{dz} = 0 \tag{17}$$

$$C_{p,l}\frac{d(W_c T_c)}{dz} = -\frac{dQ_c}{dz} = -q_c \cdot N_p \cdot 2\pi r_{pi} \tag{18}$$

$$\text{B.C.}: \; W_{h,z=0} = W_F = \rho F; \; T_{h,z=0} = T_3;$$
$$W_{f,z=0} = 0; W_{f,z=0} T_{f,z=0} = 0;$$
$$W_{c,z=l} = W_F = \rho F; \; T_{c,z=l} = T_1$$

where J (L/m^2·h) is the radial distillate flux at any location. q_h (J/m^2·h) and q_c (J/m^2·h) are the radial heat-transport fluxes from the hot feed to the falling distillate film and from the falling distillate film to the cold flow at any location, respectively.

Equations 13–18 can be numerically solved to obtain the distribution of T_h, T_c and W_f along the length of module once the radial mass and heat-transport fluxes J, q_h, and q_c are expressed as the function of radial temperature difference.

Equations for radial heat transfer

Temperature varies not only along the axial direction but also in the radial direction. Six resistances in series involving in heat transfer between hot feed and cold feed are considered. These resistances are (1) resistance of boundary layer in the lumen side of porous fiber (R_H^h), (2) resistance of porous wall filled with air (R_H^p), (3) resistance of air gap in the shell (R_H^a), (4) resistance of condensed distillate film (R_H^f), (5) resistance of dense wall (R_H^d), and (6) resistance of boundary layer in the lumen side of dense-wall fiber (R_H^c).

The heat and mass balances are also formulated below in each of the aforementioned six regions. In all enthalpy calculations, liquid water with a temperature of 0°C is taken as reference state for each process stream.

1. Within the lumen side of porous fibers q_h can be expressed as

$$q_h = \rho J C_{p,l} T_{hp} + 3600 \cdot h_h (T_h - T_{hp}) \tag{19}$$

where h_h (W/m^2·°C) is the local heat-transfer coefficient for hot flow in the lumen side of porous fibers.

2. At a location with a radius r ($r_{pi} \le r \le r_{po}$) within the porous wall

$$q_h \cdot r_{pi} = \rho J C_{p,l} T_{hp} \cdot r_{pi} + \rho J \Delta H_v(T_{hp}) \cdot r_{pi} + \rho J C_{p,v} (T_r - T_{hp}) \cdot r_{pi} - 3600 \cdot k_{pe} \frac{dT_r}{dr} \cdot r \tag{20}$$

For steady state, no accumulation of heat will occur, q_h is constant, and, thus

$$\frac{dq_h}{dr} = 0 \tag{21}$$

Combining Eq. 20, and being with the boundary conditions

$$\text{B.C.}: r = r_{pi}, T_r = T_{hp}; r = r_{po}, \; T_r = T_{pa}$$

q_h can be further expressed as[32]

$$q_h = \rho J C_{p,l} T_{hp} + \rho J \Delta H_v(T_{hp}) + \frac{\rho J C_{p,v} (T_{hp} - T_{pa})}{\left(\frac{r_{po}}{r_{pi}}\right)^{\frac{\rho J C_{p,v} r_{pi}}{3600 k_{pe}}} - 1} \tag{22}$$

where k_{pe} (W/m·°C) is the effective thermal conductivity of porous fiber wall which can be calculated by $k_{pe} = \varepsilon k_a + (1 - \varepsilon) k_p$.[18,33]

3. At a location with a thickness δ ($0 \le \delta \le \delta_a$) within the air gap

$$q_h \cdot r_{pi} = \rho J C_{p,l} T_{hp} \cdot r_{pi} + \rho J \Delta H_v(T_{hp}) \cdot r_{pi} + \rho J C_{p,v} (T_r - T_{hp}) \cdot r_{pi} - 3600 \cdot k_a \frac{dT_\delta}{d\delta} \cdot r_{po} \tag{23}$$

Similarly

$$q_h = \rho J C_{p,l} T_{hp} + \rho J \Delta H_v(T_{hp}) + \rho J C_{p,v} (T_{pa} - T_{hp}) + \frac{\rho J C_{p,v} (T_{pa} - T_{af})}{e^{\frac{\rho J C_{p,v} r_{pi} \delta_a}{3600 k_a r_{po}}} - 1} \tag{24}$$

4. Within the condensed film q_c can be expressed as

$$q_c = 3600 \cdot h_f (T_{af} - T_{fd}) \cdot \frac{N_d r_{do}}{N_p r_{pi}} \tag{25}$$

where h_f (W/m^2·°C) is the local heat-transfer coefficient for the condensed film. For the condensation of pure water vapors on the outside surface of the dense-wall fibers and falling down as laminar flow, h_f can be expressed as[34,35]

$$h_f = \left(\frac{2k^3 \rho^2 g N_d \pi r_{do}}{3\mu W_f}\right)^{1/3} \tag{26}$$

where k (W/m·°C) and μ (Pa·s) are thermal conductivity and viscosity for condensed distillate, respectively.

5. At a location with a radius r' ($r_{di} \le r' \le r_{do}$) within the dense wall

$$q_c = 3600 \cdot \frac{k_d (T_{fd} - T_{dc})}{r_{pi} \ln\left(\frac{r_{do}}{r_{di}}\right)} \cdot \frac{N_d}{N_p} \tag{27}$$

6. Within the lumen side of the dense-wall fibers

$$q_c = 3600 \cdot h_c (T_{dc} - T_c) \cdot \frac{N_d r_{di}}{N_p r_{pi}} \tag{28}$$

where h_c (W/m^2·°C) is the local heat-transfer coefficient for cold flow in the lumen side of dense-wall fibers.

Radial transport equations for mass transfer

Only two resistances involving in mass transfer are considered, which correspond to (1) resistance of porous wall (R_M^p), and (2) resistance of air gap (R_M^a), respectively.

1. Mass transfer across the porous wall.

The radial distillate flux can be written as a linear function of the vapor pressure difference[36]

$$\rho J / 3600 = \frac{p_{w,hp} - p_{w,pa}}{R_M^p} \cdot \frac{\delta_p}{r_{pi} \ln(r_{po}/r_{pi})} = K_p (p_{w,hp} - p_{w,pa}) \tag{29}$$

where δ_p is the thickness of the porous wall. $p_{w,hp}$ is the water vapor partial pressure at the interface between hot feed and porous fiber, which can be described as a function of temperature $P(T_{hp})$ from the Antoine equation[1]

$$P(T) = \exp\left(23.1964 - \frac{3816.44}{-46.13 + (T + 273.15)}\right) \quad (30)$$

R_M^p can be described by a combination of molecular diffusion, Knudsen diffusion and Poiseuille flow. Because the CEMD process is operated under atmosphere and also below 100°C, the contribution of Poiseuille flow can be neglected. The mean free path of water vapor (ca. 0.11 μm at the typical membrane temperature of 40–90°C), and the mean pore diameter of used membrane (ca. 0.2 μm) are of the same order. Therefore, both molecular and Knudsen diffusion should be taken into account.

The molecular diffusion resistance of water vapor although the stagnant air in the porous wall can be written as[36]

$$(R_M^p)_{MD} = \frac{\tau R(T_p + 273.15)\delta_p p_{\text{pln}}}{\varepsilon D_{wa}(T_p) p_0 M_{\text{w}}} \quad (31)$$

where $D_{wa}(T_p)$ is diffusion coefficient of water vapor in air which depends on temperature and can be estimated by $D_{wa}(T) = 1.895 \cdot 10^{-5}(T + 273.15)^{2.072}$,[5] p_{pln} is the logarithm mean of the air pressure at both sides of the porous fiber at any location, and T_p is the average temperature across the porous fiber at any location, $T_p = (T_{hp} + T_{pa})/2$, °C.

The Knudsen diffusion resistance of water vapor through the porous wall by a series of molecular-wall collision can be written as[36,37]

$$(R_M^p)_{Kn} = \frac{3\tau\delta_p}{d_p\varepsilon}\sqrt{\frac{\pi R(T_p + 273.15)}{8M_W}} \quad (32)$$

Thus, R_M^p in Eq. 29 can be summarized as below by electrical circuit analogy

$$R_M^p = (R_M^p)_{MD} + (R_M^p)_{Kn} \quad (33)$$

2. Mass transfer across the air gap.

Molecular diffusion of vapor through the stagnant air gap is known as Stefan diffusion and is given by[9]

$$N_w \cdot r_{pi} = \frac{\rho J}{3600M_w} \cdot r_{pi} = -D\frac{dc_w}{d\delta} \cdot r_{po} + x_w(N_w + N_a) \cdot r_{pi} \quad (34)$$

where N_w and N_a (mol/m^2·s) are the radial mole fluxes for water vapor and air, respectively. c_w (mol/m^3) and x_w are the concentration and mole fraction of water vapor, respectively.

For $N_a = 0$ and ideal gas $c_w = p_w R\ (T + 273.15)$, Eq. 34 becomes

$$\rho J/3600 = -\frac{p_0 D(T_\delta) M_w}{R(p_0 - p_{w,\delta})} \cdot \frac{d(p_{w,\delta}/(T_\delta + 273.15))}{d\delta} \cdot \frac{r_{po}}{r_{pi}} \quad (35)$$

$$\text{B.C.}: \delta = 0, p_w = p_{w,pa}; \delta = \delta_a,\ p_w = p_{w,af} = P(T_{af})$$

Actually, T_δ varies with δ and the relation is approximately linear. For the convenience of calculation, T_δ in Eq. 35 is substituted by the arithmetic mean temperature in the air gap $T_a = (T_{pa} + T_{af})/2$.[33] Thus

$$\rho J/3600 = \frac{p_0 D_{wa}(T_a) M_w}{\delta_a R(T_a + 273.15)} \ln\left(\frac{p_0 - p_{w,af}}{p_0 - p_{w,pa}}\right)\frac{r_{po}}{r_{pi}} = K_a(p_{w,pa} - p_{w,af}) \quad (36)$$

Numerical methods

Governing Eqs. 13–18 along with radial transport Eqs. 19, 22, 24, 25, 27–29, and 36 constitute a set of 14 nonlinear coupled ordinary differential equations (ODEs).To numerically solve the aforementioned equations, the length of module is divided into n slices as depicted in Figure 5a, and each slice has a step length of l/n. A step length of around 2.5 μm is sufficient for the inaccuracy of results less than 0.01%. T_h and T_c could be considered constant within each slice. For the first slice, $T_{h,1st} = T_{h,z} = 0$, and an initial guess of $T_{c,z} = 0$ (T_2) is required so $T_{c,1st} = T_{c,z} = 0$. Similarly at the ith ($1 \le i \le n$) slice, $T_{h,ith} = T_{h,z=(i-1)l/n}$ and $T_{c,ith} = T_{c,z=(i-1)l/n}$. The temperature of distillate leaving from the ith slice ($T_{f,z=il/n}$), as depicted in Figure 4, follows directly from $T_{af,ith}$ and $T_{fd,ith}$. Thus, $T_{f,z=il/n}$ can be derived as the arithmetic average

$$T_{f,z=il/n} = (T_{af,ith} + T_{fd,ith})/2 \quad (37)$$

Once $T_{h,ith}$ and $T_{c,ith}$ are known, Eqs. 19, 22, 24, 25, 27–29 and 36 along with Eqs. 15, 16 and 37, which are used to correlate the relationship between q_h and q_c can be manipulated to yield a set of 11 nonlinear equations for each of following 11 unknown variables $q_{h,ith}$, $q_{c,ith}$, J_{ith}, $T_{hp,ith}$, $T_{pa,ith}$, $T_{af,ith}$, $T_{fd,ith}$, $T_{dc,ith}$ and $p_{w,pa,ith}$, as well as flow rate and temperature of the distillate leaving from the ith slice $W_{f,z=il/n}$ and $T_{f,z=il/n}$. Since J_{ith}, $q_{h,ith}$ and $q_{c,ith}$ are known, Eqs. 13, 14, 17 and 18 could be solved for $T_{h,z=il/n}$ (= $T_{h,(i+1)th}$) and $T_{c,z=il/n}$ (= $T_{c,(i+1)th}$). Calculation is continued slice by slice. At the last slice, the obtained $T_{c,z=l}$ is compared with the set boundary condition (T_1). If the difference is greater than the maximum acceptable one (determined as 0.008°C), a new initial guess of $T_{c,z} = 0$ (T_2) is performed and the calculation of iteration proceeds until $T_{c,z=l}$ satisfies the convergence criteria. J_D is obtained by

$$J_D = W_{f,z=l}/S_{pi} = \left(\sum_{i=1}^{n} J_{ith}\right)/n \quad (38)$$

A simulation program was developed with Matlab® (version R2010a, MathWorks, Inc., USA). The calculation scheme for modeling of the CEMD process and the used built-in routine in Matlab® are presented in Figure 5b.

Experimental

Membrane, modules and heat exchangers

Two modules with different types of membranes were used. The porous PP membrane fibers were from Accurel MEMBRANA (Wuppertal, Germany): they were identified as PP Q3/2 and PP 150/330. The dense-wall PP fibers were provided by Chembrane Engineering and Technology, Inc., Tianjin, China. Two modules, Module 1 and Module 2, were fabricated at Chembrane Engineering and Technology, Inc., Tianjin, China. Geometric characteristics of two modules and three types of fibers are listed in Table 1. The

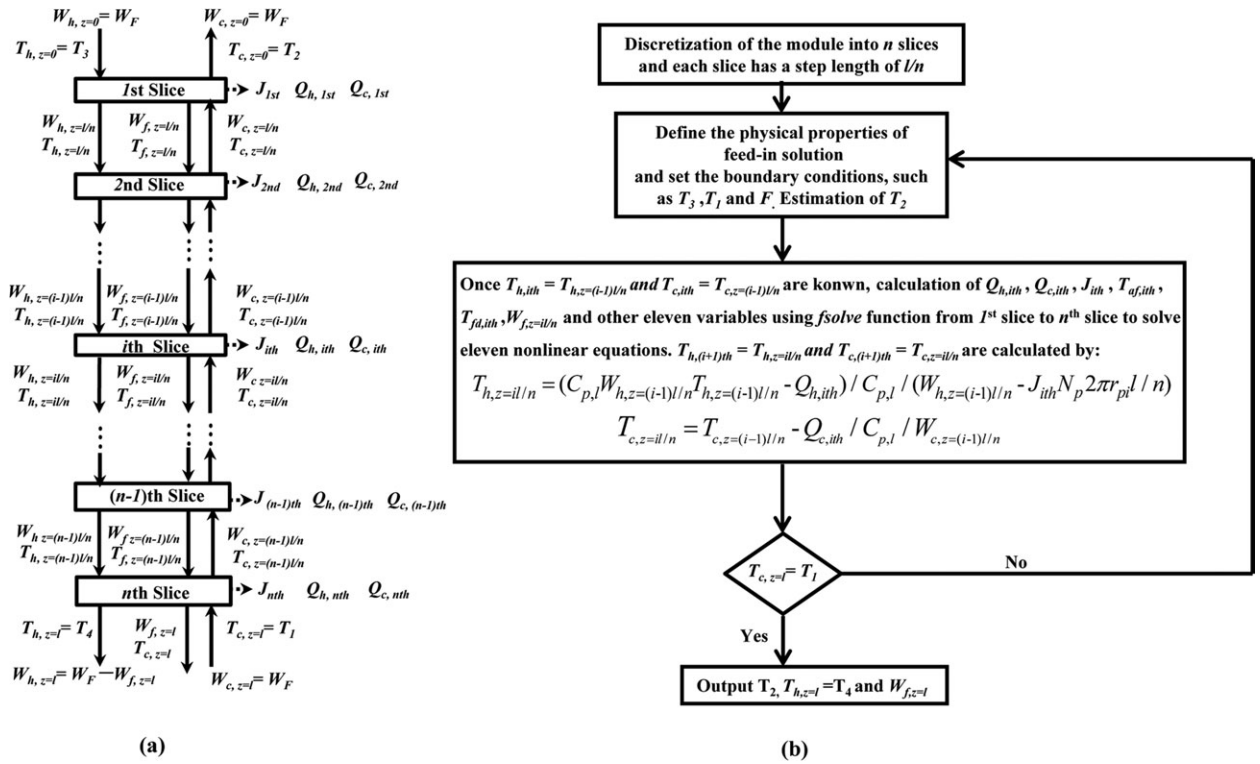

Figure 5. Calculation scheme for simulation of CEMD process.

configuration parameters for each module were decided arbitrarily just to illustrate this process. Three external heat exchangers, HX1, HX2 and HX3 provided by Chembrane Engineering and Technology, Inc., Tianjin, China, were built out of dense-wall PP fibers, which are the same with ones that were used in CEMD modules.

Experimental setup

The experimental setup is schematically depicted in Figure 6. The module was placed vertically during the operation, which had been pressure-tested by pure water to assure no leakage. Aqueous solution of 0.2 wt % NaCl with the conductivity of around 3,000 μS/cm was used as a feed solution whose vapor pressure is approximately equal with that of pure water. The salt in the feed solution mainly acts as a tracer. Therefore, we could check any leakage in the module or the external heat exchangers during the experiment by detecting the conductivity of the distillate. The feed solution was prepared in the thermostat A (Scientz Biotechnology, Ltd., Ningbo, China), which maintained a constant temperature at 25–45°C within ±0.1°C. It was then introduced to the inlet of dense-wall fibers by a magnetic chemical resistant centrifugal pump (Speedmind Electro-mechanical, Ltd., Hong Kong, China), and the circulation rate was controlled by a rotameter with a maximum capacity of 54 L/h, which was also calibrated by using a stop watch and measurement cylinder. The feed solution at the outlet of dense-wall fibers went through the lumen side of two external heaters (HX1 and HX2) in series, and meanwhile was countercurrently heated by hot water from thermostat B (Scientz Biotechnology, Ltd., Ningbo, China). The inlet temperature of the porous fibers was kept constant at 70–90°C within ±0.1°C by manipulating the temperature setting of thermostat B and flow rate of hot water through the shell side. The position of the exit of the tubing connected to the outlet of the porous fibers was lifted to a level as high as the top of the module to assure that the lumen of all the porous fibers could be fully filled with solution. After leaving the module, the feed was allowed to flow although the lumen side of another external heat exchanger (HX3) and was countercurrently cooled by the cold water

Table 1. Details of the Fibers, Modules Used for CEMD Process

Particulars	Module 1	Module 2
Effective length of module, l (m)	0.62	1.07
Shell inside diameter, d_s (mm)	35	35
Support porous fiber type	PP Q3/2	PP 150/330
Number of porous fibers, N_p	310	564
Porosity, ε	0.75*	0.65‡
Average pore size, d_p, μm	0.20**	0.20**
Tortuosity, τ	2.0*	2.0*
Inner diameter of porous fibers, d_{pi} (mm)	0.6**	0.33**
Wall thickness of porous fibers, δ_p (mm)	0.2**	0.15**
Number of dense-wall fibers, N_d	620	846
Inner diameter of dense-wall fibers, d_{di} (mm)	0.38**	0.38**
Wall thickness of dense-wall fibers, δ_d(mm)	0.05**	0.05**
Effective evaporation surface area, S_{pi} (m^2)	0.362	0.625
Effective condensation surface area, S_{do} (m^2)	0.604	1.421
N_d/N_p	2:1	1.5:1
S_{do}/S_{pi}	1.67	2.27
Packing density, φ	0.38†	0.35†

*From Ref. 37.
**From manufacturer.
†The packing density (φ) is calculated from $\varphi = (N_p d_{po}^2 + N_d d_{do}^2)/d_s^2$.
‡From Ref. 7.

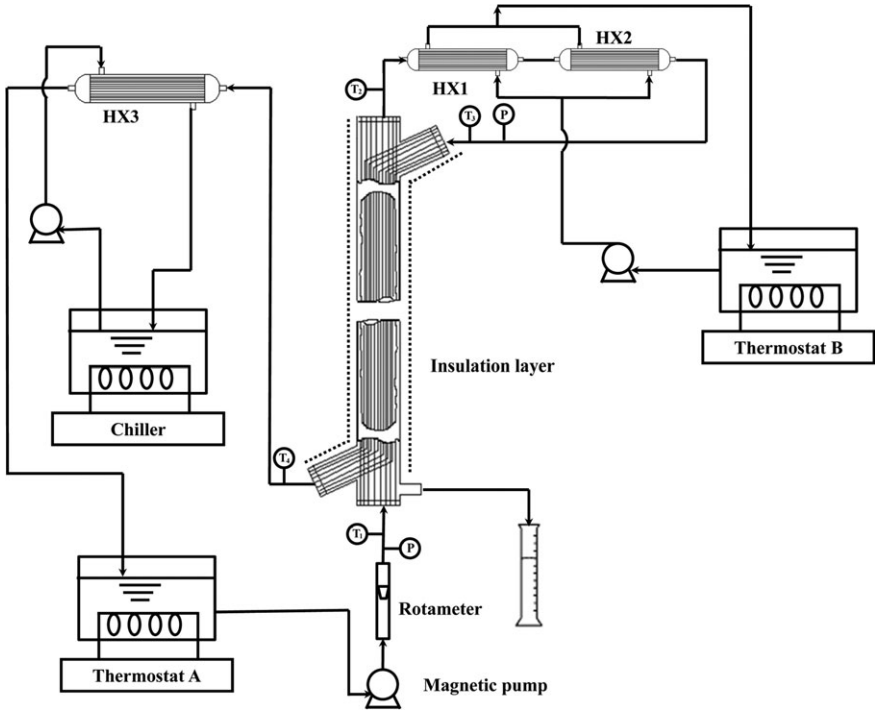

Figure 6. Schematic diagram of the experimental setup for CEMD process.

from a chiller (Xutemp, Ltd., Hangzhou, China), and then flowed back into the thermostat A.

Insulation of the module body and feed-carrying-tubings could effectively form a heat conduction barrier between the system and the surrounding. The temperatures of the feed solution at four points (two inlets and two outlets) were measured with Pt100 thermometers (Cole-Parmer, Vernon Hills, USA). After calibration their mutual deviation was less than 0.1°C. The inlet pressure of both fibers was monitored by pressure gauges (0–0.1 MPa). The inlet pressure of porous fibers is particularly assured no more than 0.1 MPa (gauge pressure) to avoid membrane wetting. After the whole system was running at steady state, the distillate permeation rate was measured by a volumetric cylinder read every 6–10 min.

Each experiment was repeated at least twice under the same operational condition, the data reported being the average values.

Experimental design

There are three independent process inputs: T_1, T_3 and F. The provided heat source is below 95°C. The operational conditions in this study were carried out as below: T_1 was preset at a value between 25–45°C. T_3 was preset at a value between 70–90°C. The range of F was preset at a value between 16–48 L/h.

Considering the interaction effect between the inputs, response surface method (RSM) can be used to find the relationship between responses and inputs by experimental design, which was successfully applied to the DCMD, AGMD and OD processes.[38–40] In this study, the face-centered central composite design, a cubic design, was chosen for selecting experimental points in the region of interest. For three variables T_1, T_3 and F were coded according to the following equations

$$Z_1 = \frac{T_1 - 35}{10}, Z_2 = \frac{T_3 - 80}{10}, Z_3 = \frac{F - 32}{16} \tag{39}$$

The coded and real levels of the independent operating variables are listed in Table 2. The designation of experimental points, analysis of variance (ANOVA), and RSM regression were carried out by Minitab® (version 15, Minitab, Inc., USA).

Experimental procedure for concentration of dilute aqueous sugar solution

When concentrating the aqueous sugar solution, the feed was prepared in a 12 L reservoir instead of thermostat A, as a large amount of water loss during concentration cannot guarantee that the heating coil in the thermostat is always immersed in the solution. The inlet temperature of dense-wall fibers was adjusted by both the preset temperature of the chiller and the flow rate of the cooling water. The initial concentration of artificial cellulosic hydrolysate is 12 g/L glucose and 6 g/L xylose.

The concentrations of glucose and xylose in the distillate and feed reservoir were determined by a HPLC system (2515 pump and 2410 refractive index detector,Waters,

Table 2. Independent Variables and Their Values for Face-centered Central Composite Design

	Real values of coded levels		
Variable	−1	0	+1
Inlet temperature of dense-wall fibers, T_1(°C)	25	35	45
Inlet temperature of porous fibers, T_3(°C)	70	80	90
Circulation rate, F (L/h)	16	32	48

Table 3. Experimental Results of Face-centered Central Composite Experimental Design

				Response									
	Input factors			Module 1					Module 2				
Standard order	T_1(°C)	T_3(°C)	F(L/h)	J_D(L/m^2·h)	R	T_2(°C)	PR	η	J_D(L/m^2·h)	R	T_2(°C)	PR	η
1	25.0	70.0	16.0	2.155	4.9%	63.1	3.98	0.721	1.36	5.3%	66.0	7.49	0.731
2	45.0	70.0	16.0	1.49	3.4%	66.8	5.89	0.864	0.934	3.6%	67.9	9.71	0.891
3	25.0	90.0	16.0	3.53	8.0%	81.0	4.94	0.795	2.14	8.4%	85.3	9.93	0.774
4	45.0	90.0	16.0	2.96	6.7%	85.4	8.04	0.916	1.85	7.2%	87.1	13.80	0.949
5	25.0	70.0	48.0	5.23	3.9%	56.5	1.64	0.702	3.75	4.9%	61.5	3.23	0.753
6	45.0	70.0	48.0	3.71	2.8%	63.8	2.52	0.830	2.54	3.3%	66.1	4.69	0.875
7	25.0	90.0	48.0	9.20	6.9%	73.2	2.29	0.797	5.77	7.5%	80.4	4.32	0.754
8	45.0	90.0	48.0	7.34	5.5%	79.9	3.02	0.873	4.80	6.3%	84.6	6.41	0.871
9	25.0	80.0	32.0	5.26	6.0%	68.5	2.89	0.764	3.24	6.3%	72.9	4.99	0.740
10	45.0	80.0	32.0	4.04	4.6%	73.1	3.67	0.902	2.50	4.9%	76.1	7.04	0.872
11	35.0	70.0	32.0	3.43	3.9%	62.2	2.79	0.799	2.23	4.4%	65.5	5.47	0.799
12	35.0	90.0	32.0	6.14	6.9%	79.8	3.77	0.858	3.72	7.3%	84.1	6.82	0.820
13	35.0	80.0	16.0	2.59	5.9%	73.5	5.03	0.849	1.65	6.4%	76.6	10.60	0.864
14	35.0	80.0	48.0	6.29	4.7%	68.1	2.22	0.796	4.30	5.6%	73.3	4.66	0.815
15	35.0	80.0	32.0	4.64	5.2%	70.9	3.21	0.814	2.95	5.8%	74.8	6.21	0.808
16	35.0	80.0	32.0	4.69	5.3%	70.8	3.21	0.825	2.94	5.7%	74.9	6.28	0.803
17	35.0	80.0	32.0	4.80	5.4%	71.1	3.40	0.837	3.10	6.1%	75.0	6.76	0.844
18	35.0	80.0	32.0	4.64	5.2%	71.3	3.36	0.805	2.90	5.7%	75.2	6.58	0.786
19	35.0	80.0	32.0	4.79	5.4%	70.7	3.24	0.845	2.98	5.8%	74.9	6.37	0.814
20	35.0	80.0	32.0	4.68	5.3%	70.9	3.24	0.821	2.96	5.8%	74.6	5.97	0.814

USA) using a Biorad Aminex HPX-87H column (Biorad, Hercules, USA) at 65°C with 5 mmol H_2SO_4 as the mobile phase at a flow rate of 0.6 mL/min.

Results and Discussion

System performance and response surface analysis

The experimental results of performance indicators with T_1, T_3 and F for both modules using 0.2 wt % NaCl aqueous solution as the feed by a face-centered central composite design are shown in Table 3. In all cases, the conductivity of distillate was under 3 μS/cm, i.e., the rejection factor is higher than 99.9%, which was independent on operating conditions. As shown in Table 3, the flux varied between 1.49–9.20 L/m^2·h for Module 1, and between 0.934–5.77 L/m^2·h for Module 2 over the studied experimental range. Fractional recovery for both modules was around 2.8–8.4% (<9%), which increases with the increase of T_3 and with the decrease of T_1 and F. The experimental data of ΔT_{top} were in the range of 3.2–16.8°C for Module 1, and 2.1–9.6°C for Module 2. The PR calculated by Eq. 8 reached a value of 1.64–8.04 for Module 1 and 3.22–13.8 for Module 2. The evaporation efficiency calculated by Eq. 11 ranged from 0.702 to 0.916 and 0.731 to 0.947 for Module 1 and Module 2, respectively. These high values of PR and η have shown the advantages of CEMD process. In general, Module 1 has a larger flux, and Module 2 has a higher PR under the same operation condition.

Using the aforementioned 20 runs given in Table 3, a second-order polynomial regression for output (J_D or T_2) and inputs (T_1, T_3 and F) relation was also established as the following (in terms of coded levels)

$$J_D = \beta_0 + \beta_1 Z_1 + \beta_2 Z_2 + \beta_3 Z_3 + \beta_{12} Z_1 Z_2 + \beta_{13} Z_1 Z_3 + \beta_{23} Z_2 Z_3 + \beta_{11} Z_1^2 + \beta_{22} Z_2^2 + \beta_{33} Z_3^2 \quad (40)$$

$$T_2 = \gamma_0 + \gamma_1 Z_1 + \gamma_2 Z_2 + \gamma_3 Z_3 + \gamma_{12} Z_1 Z_2 + \gamma_{13} Z_1 Z_3 + \gamma_{23} Z_2 Z_3 \quad (41)$$

Multiple regression coefficients were obtained using a least-squares technique. ANOVA is summarized in Tables 4 and 5 for the two regression equations. A large absolute t value and

Table 4. Coefficients Corresponding to RSM Regression for J_D

	Module 1			Module 2		
Coefficient	Value	t-value	P-value*	Value	t-value	P-value
β_0	4.708	173.50	<0.0001	2.969	173.18	<0.0001
β_1	−0.584	−23.38	<0.0001	−0.364	−23.05	<0.0001
β_2	1.316	52.70	<0.0001	0.747	47.34	<0.0001
β_3	1.905	76.30	<0.0001	1.323	83.86	<0.0001
β_{12}	−0.031	−1.10	0.2982	0.047	2.67	0.0237
β_{13}	−0.268	−9.61	<0.0001	−0.183	−10.38	<0.0001
β_{23}	0.594	21.30	<0.0001	0.323	18.32	<0.0001
β_{11}	−0.060	−1.27	0.2345	−0.096	−3.18	0.0098
β_{22}	0.075	1.57	0.1473	0.009	0.31	0.7642
β_{33}	−0.270	−5.68	0.0002	0.009	0.31	0.7642
R^2	0.999			0.999		
Predicated R^2	0.9981			0.992		
Adjusted R^2	0.9887			0.9975		
Lack of fit			0.349			0.9948
Regression			<0.0001			<0.0001

*P<0.001: highly significant; 0.001≤P<0.01: significant; P≥0.01: non-significant.

Table 5. Coefficients Corresponding to RSM Regression for T_2

	Module 1			Module 2		
Coefficient	Value	t-value	P-value*	Value	t-value	P-value
γ_0	71.03	975.23	<0.0001	74.84	1612.24	<0.0001
γ_1	2.67	25.92	<0.0001	1.57	23.92	<0.0001
γ_2	8.69	84.37	<0.0001	9.45	143.95	<0.0001
γ_3	−2.83	−27.47	<0.0001	−1.70	−25.90	<0.0001
γ_{12}	0.0125	0.11	0.9152	−0.0625	−0.85	0.4099
γ_{13}	0.7375	6.40	<0.0001	0.6375	8.69	<0.0001
γ_{23}	−0.4625	−4.02	0.0015	−0.1375	−1.87	0.0837
R^2	0.9985			0.994		
Predicated R^2	0.9978			0.991		
Adjusted R^2	0.9907			0.9989		
Lack of fit			0.1178			0.4691
Regression			<0.0001			<0.0001

*P<0.001: highly significant; 0.001≤P<0.01: significant; P≥0.01: non-significant.

a small P value for each coefficient would indicate its significant effect on the response. From Tables 4 and 5, it is observed that for both modules the factors with high-significant effect on the flux are F, T_3 and T_1, followed by the interactions between T_3 and F, and at last the interaction between T_1 and F. The interaction between T_3 and F increases the flux, while the interaction between T_1 and F decreases the flux. The variables with high-significant effect on T_2 for both modules are T_3, F and T_1, followed by the interaction between T_1 and F. The regression equations to predict J_D and T_2 were quite highly significant (P < 0.0001), and suitable as indicated by the lack of fit analysis (P ≥ 0.01: nonsignificant relative to the pure error). The coefficient of determination (R^2), adjusted coefficient of determination (adjusted-R^2), and predicted coefficient of determination (predicated-R^2), were all >0.98, indicating the quadratic equations were adequate to predict the corresponding experimental data.

The contour-line plots for J_D and PR predicted by regression equations are shown in Figure 7 for Module 1 and Figure 8 for Module 2. It is obvious that performance of both modules shows the same monotonic behavior with the change of operating variables. It can be seen that J_D increases with the increase of either T_3 or F, and decreases with the increase of T_1. PR increases with the increase of either T_1 or T_3, and decreases with the increase of F. The trends are the same with other modules or processes with heat recovery.[14,17] There exists a tradeoff between J_D and PR, that is, there is no certain operating condition to obtain the maximum of both PR and J_D. In the studied condition range, the predicted maximum J_D was achieved under T_1 = 25°C, T_3 = 90°C, and F = 48 L/h, with a value of 9.15 L/m^2·h for Module 1 and 5.78 L/m^2·h for Module 2. The maximum PR was obtained under T_1 = 45°C, T_3 = 90°C, and F = 16 L/h, with a value of 7.25 for Module 1 and 13.37 for Module 2. These predictions were

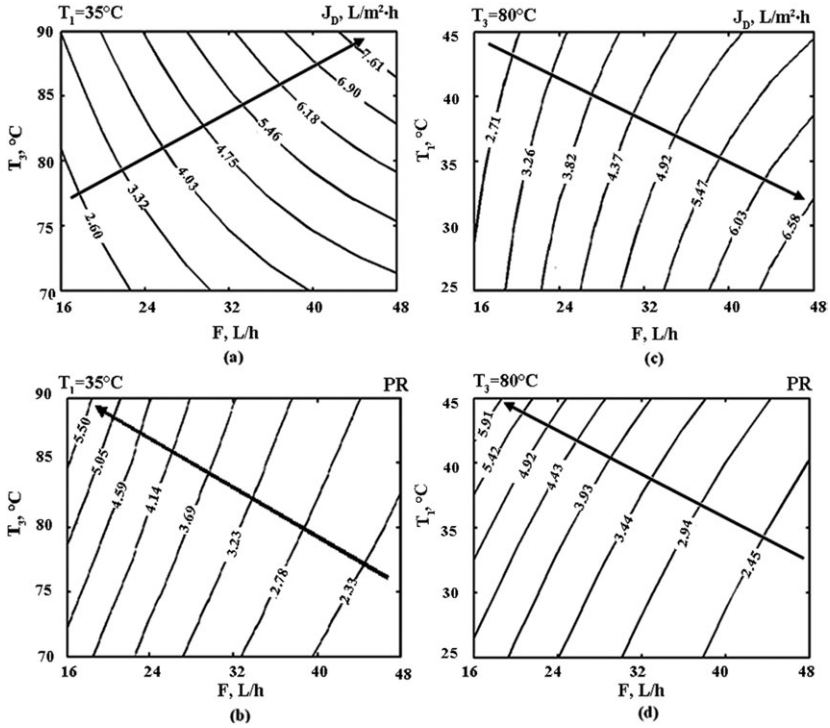

Figure 7. Contour plots for (a) J_D, and (b) PR as a function of T_3 and F at fixed T_1 = 35°C, and for (c) J_D, and (d) PR as a function of T_1 and F at fixed T_3 = 80°C using Module 1.

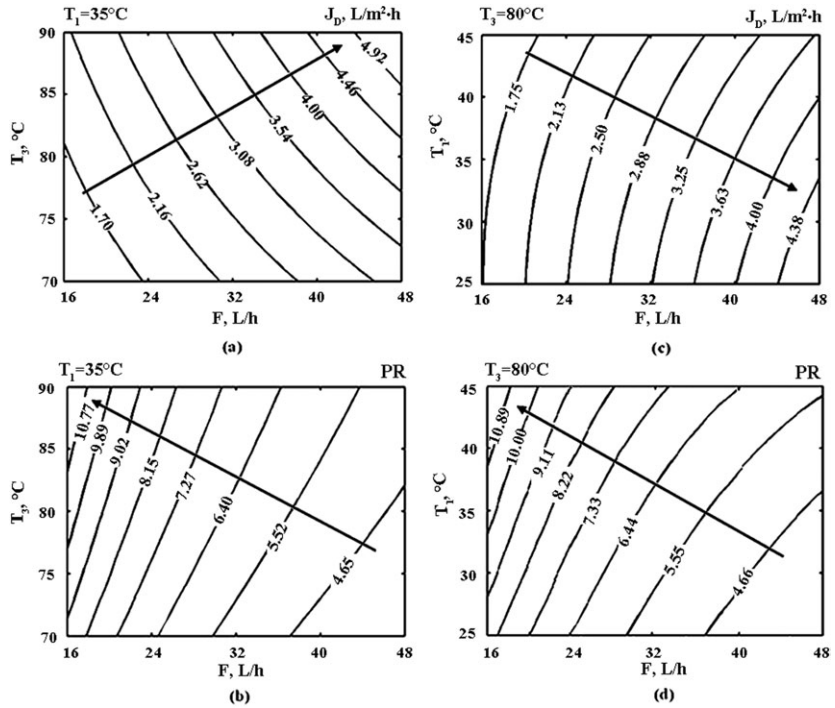

Figure 8. Contour plots for (a) J_D, and (b) *PR* as a function of T_3 and F at fixed $T_1 = 35°C$, and for (c) J_D, and (d) *PR* as a function of T_1 and F at fixed $T_3 = 80°C$ using Module 2.

authenticated by experimental observations. It is necessary to maintain a high value of *PR,* and meanwhile a suitable production rate of pure water for a CEMD system in a practical application, thus, a large area of membrane which acts as the evaporation interface should be provided. The price of suitable membrane would be a determinant for application of CEMD process in the industrial scale.

Estimation of heat- and mass-transfer coefficients under the operation conditions

The local heat-transfer coefficients for both hot flow and cold flow can be calculated from the respective local Nusselt number (*Nu*), which is defined as

$$Nu_h = h_h d_{pi}/k_h \tag{42}$$

$$Nu_c = h_c d_{di}/k_c \tag{43}$$

where k_h and k_c are the thermal conductivities of hot and cold flow, respectively.

The flow pattern for both flows is laminar indicated by the Reynolds number in our experimental study ranging from 29.3 to 232.5. Because the entrance length for hydrodynamic development is far smaller than the length of two arms where fibers were situated in the potting, calculation of *Nu* is based on fully developed laminar flow. For long and thin fibers were used, the Graetz number was about 0.04–0.57 (< 1), which means the entrance length for thermal development is also far smaller than the fiber length, and, thus, the thermal boundary could be considered as fully developed. For relative small radial permeation rate, Nu_h and Nu_c can be estimated as 4.0,[32,41,42] which is an average of $Nu = 3.66$ (for constant wall temperature), and $Nu = 4.36$ (for constant flux).

Calculation of δ_a by the geometrical approach according to Eq. 12 yielded a value of 4.12×10^{-4}m for Module 1 and 3.63×10^{-4}m for Module 2. This geometric method is valid only for the ideal fiber arrangements as shown in Figure 3a–d. The correct δ_a should be determined by several assumed values that bring the numerical solutions of the ODEs to a good agreement with the observed data. δ_a was, thus, obtained by this trial and error method as 4.85×10^{-4}m for Module 1, and 6.85×10^{-4}m for Module 2, which are close to and in the same order of magnitude with the value of δ_a obtained by geometrical method.

The local mass-transfer coefficient for porous wall, K_p, depends on the characteristics of porous fiber and also thermal conditions across the wall, which will vary in the axial direction of the module. K_p was calculated by Eq. 29 at each slice along the module length under different operation conditions when fixing the value of τ, ε and r_p for porous fiber listed in Table 1. The maximum temperature difference across the porous wall ($T_{hp} - T_{pa}$) along the module length was no more than 3.0°C, thus, local K_p is plotted with local T_p in Figure 9. It can be seen that K_p for PP 150/330 is higher than that for PP Q3/2, and both increase with the increasing T_p. It is also evident that for a certain membrane, K_p is only the function of T_p and almost independent of the outside operation conditions. Compared with the reported K_p in earlier articles, e.g., $K_p = 2.53 \times 10^{-7} kg/m^2 \cdot Pa \cdot s$ at 25°C for PP Q3/2[43] and $K_p = 5.0\text{–}6.1 \times 10^{-7} kg/m^2 \cdot Pa \cdot s$ at 85–90°C for PP 150/330,[44] the calculated values agree with them.

Experimental verification of the theoretical model prediction

Experimental results of the steady state value of J_D, T_3-T_2, *PR* and η besides the aforementioned 20 runs were used to verify the theoretical model. The performance indicators with the variation of one operating variable when the other variables were kept constant are both theoretically and

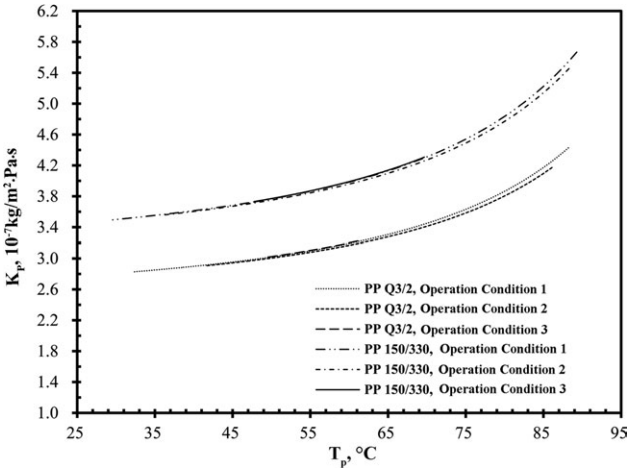

Figure 9. K_p vs. T_p at three operation conditions using two membranes.

Operation condition 1: $T_1 = 25°C$, $T_3 = 90°C$ and $F = 16$ L/h; operation condition 2: $T_1 = 25°C$, $T_3 = 90°C$ and $F = 48$ L/h; operation condition 3: $T_1 = 45°C$, $T_3 = 70°C$ and $F = 32$ L/h.

experimentally shown in Figures 10–12 for both modules. The theoretical flux agreed quite well compared with the experimental ones within the maximum relative error of 6.5%. The difference between theoretical and experimental data of ΔT_{top} was in the range of 0.0–1.5°C; most of them were around 0.1–0.5°C. The *PR* and η calculated from theoretical values also described the observed behavior quite well. In accordance with the previous RSM regression, the relation between performance indicators and operating variables was monotonic. It also can be seen in Figures 10d–12d that η increases with the increase of T_1 and T_3, and F has little effect on it. An increase of T_1 has more of an effect on η than an increase of T_3. Thus, high *PR* usually means high-evaporation efficiency.

In some experimental points, there was an obvious difference between the experimental and theoretical values for *PR* and η, e.g., for Module 2 the model predicted a higher *PR* of 18.3 than the experimental one of 13.8, and a lower η of 0.876 than the experimental one of 0.949. There are two reasons for a prediction of higher *PR* and lower η: one is that *PR* mainly depends on ΔT_{top}. When a high *PR* is obtained, the value of ΔT_{top} is quite small, such as 2-3°C. Even if a small observed error of 0.2–0.5°C happened, it would cause a relative error as high as 20% for calculation. The other reason is that possible heat loss to the relative cold surrounding that is not accounted for in the previously described model. Although both modules were well insulated in the experiment, they were still not ideally adiabatic. Especially under a small circulation rate, high temperature of feed-in and potential large heat-exchanging area to the surrounding, the amount of heat loss would be inevitably enlarged. As shown in Figure 4, if the heat loss exists, when the heat is being transferred across the air gap, an amount of the heat would go to inside surface of the shell either by conduction or vapor condensation driven by temperature difference. When considering the heat loss, the governing Eq. 16 should be changed into

$$C_{p,l}\frac{d(W_f T_f)}{dz} = \frac{d(Q_h - Q_c - Q_{loss})}{dz} = (q_h - q_c - q_{loss}) \cdot N_p \cdot 2\pi r_{pi} \tag{44}$$

It is very difficult to measure Q_{loss}. Suppose $Q_{loss} = 3\%Q_h$, and the lost -heat-carrying vapor was totally condensed,

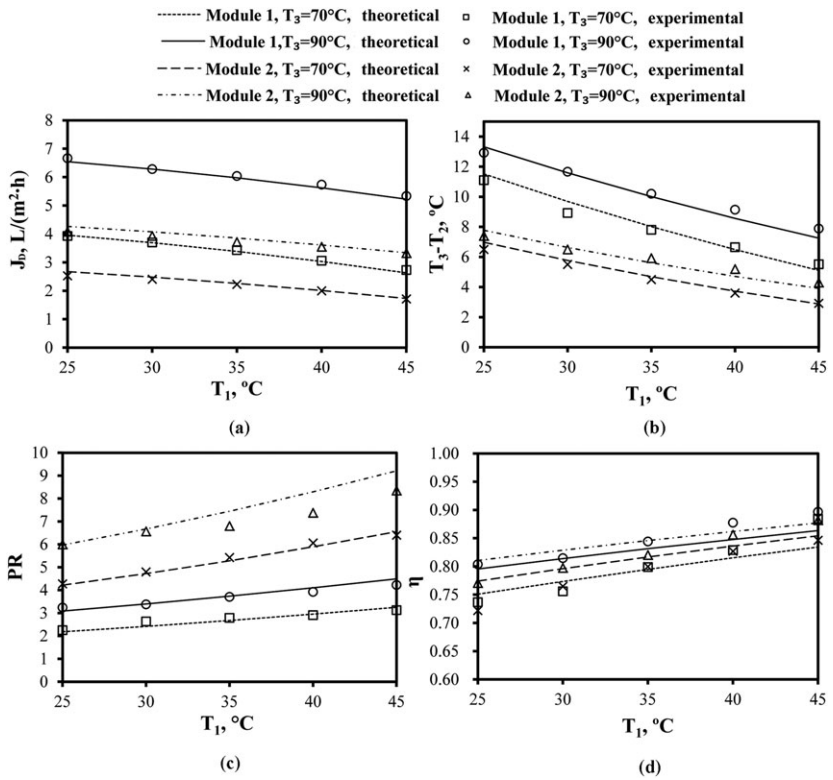

Figure 10. Experimental and theoretical values of (a) J_D, (b) T_3–T_2, (c) *PR*, and (d) η with T_1 under $F = 32$ L/h at $T_3 = 70°C$ and $T_3 = 90°C$ using both modules.

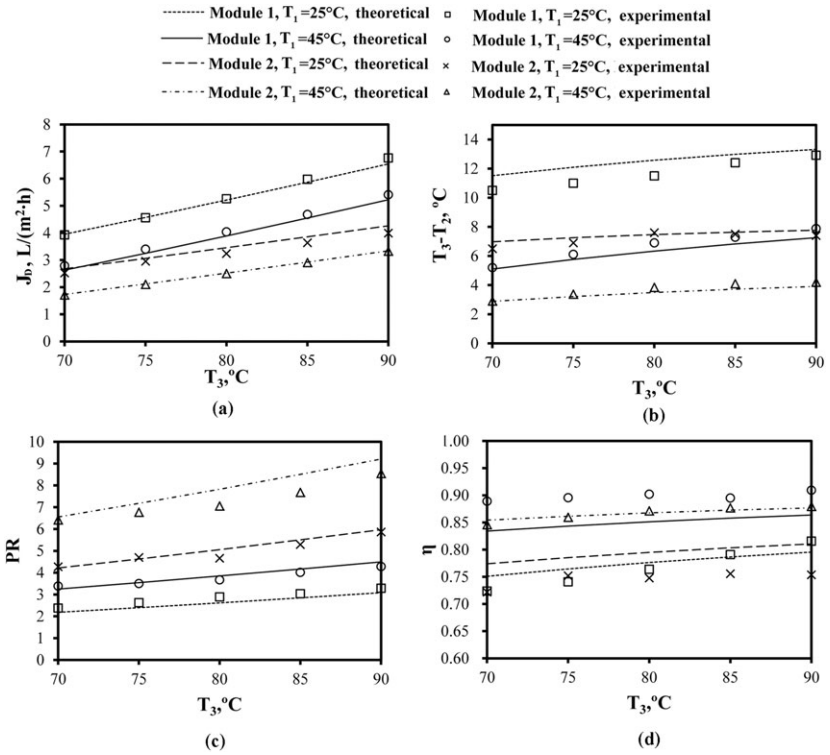

Figure 11. Experimental and theoretical values of (a) J_D, (b) T_3–T_2, (c) PR, and (d) η with T_3 under F = 32 L/h at T_1 = 25°C and T_1 = 45°C using both modules.

Table 6 shows the comparison of the experimental data, theoretical ones with and without considering heat loss. It can be seen that the model when considering heat loss describes well the experimental data. From Table 6, heat loss did decrease PR and increase nominal η that was calculated by Eq. 11, which is different from the actual one that should be calculated by Eq. 10. As mentioned in the previous section, due to heat loss, ΔT_{top} became larger than ΔT_{bottom}, which was in

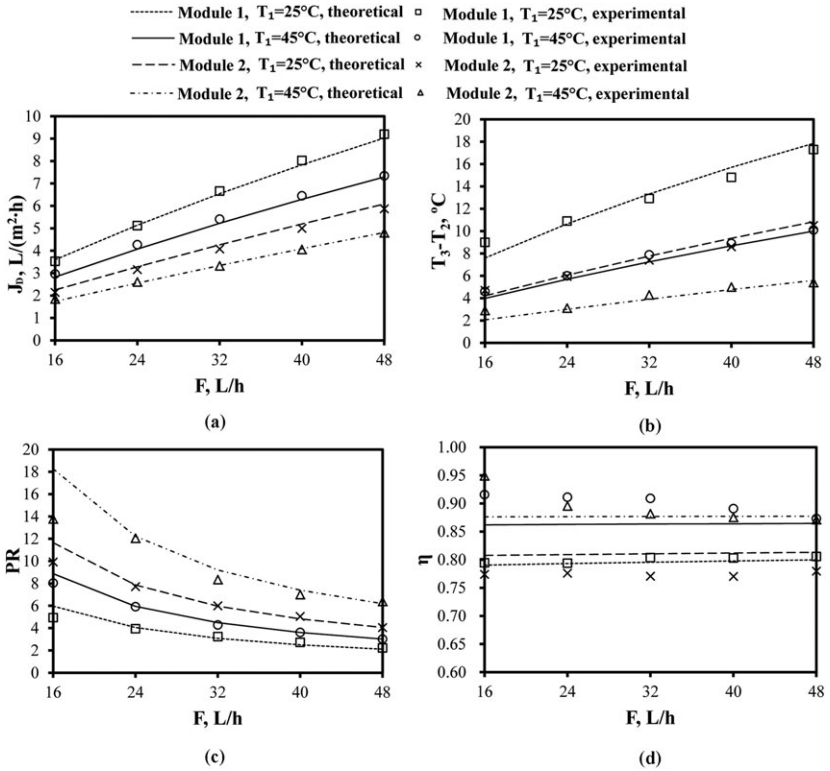

Figure 12. Experimental and theoretical values of (a) J_D, (b) T_3–T_2, (c) PR, and (d) η with F under T_3 = 90°C at T_1 = 25°C and T_1 = 45°C using both modules.

Table 6. Comparison of Experimental, Theoretical Results with and without Considering Heat Loss

Operation Condition	J_D (L/m^2·h)	T_2 (°C)	T_4 (°C)	ΔT_{top} (°C)	ΔT_{bottom} (°C)	*PR*	Nominal η	Actual η
A* (Experimental)	1.85	87.10	46.90	2.90	1.90	13.8	0.949	n.d.‡
A (Theoretical, 3%†)	1.82	86.99	46.70	3.01	1.72	13.1	0.938	0.907
A (Theoretical, 0%)	1.74	87.94	47.19	2.06	2.19	18.3	0.876	0.876
B** (Experimental)	0.93	67.90	46.70	2.10	1.72	9.7	0.891	n.d.
B (Theoretical, 3%)	0.96	67.985	46.60	2.01	1.61	10.4	0.914	0.885
B (Theoretical, 0%)	0.92	68.47	46.59	1.53	1.58	13.1	0.876	0.876

*Operation condition A: T_1=45°C, T_3=90°C, F=16L/h.
**Operation condition B: T_1=45°C, T_3=70°C, F=16L/h.
†Heat loss percent in Q_h.
‡Not determined.

accordance with the experimental observation. For the environment acts as another cold side when heat loss exists, the experimental flux was higher than the theoretical one without heat loss. These results showed that 3% heat loss would lead to nearly 30% decrease of *PR*. In a practical application, well insulation of the whole system should be guaranteed.

Effect of operating variables on axial temperature and flux distribution

The effect of T_1, T_3 and F on the flux and temperature drop along the module length is elucidated in a local view, as shown in Figure 13a–c. The temperature drop in both hot and cold flow and also the flux are much larger at the upper part of the module than that at the lower part of the module, which means that a large proportion of heat and mass transfer occurs at the upper part. This is mainly owing to the relative high level of T_h, which is kept at the upper part. Both high K_p and K_a are achieved at high T_h. Additionally, the overall driving force, i.e., $p_{w,hp}$-$p_{w,af}$, depends on not only the temperature difference (T_h –T_c), but also on the temperature level of the hot side (T_h).

As shown in Figure 13a, the local flux obtained at z = 0.62 m (the bottom of Module 1) at 25 and 45°C would be nearly equal, although T_h –T_c at 25°C is larger than that at 45°C. Thus, high T_h may more or less offset the effect of a small temperature difference on the flux. This also explains that by lifting T_h –T_c why the effect of increasing T_3 is much stronger than that of lowering T_1 on the flux, as shown in Figures 10a and 11a. Change of the flow rate would affect the axial temperature distribution, as shown in Figure 13c. At a smaller F which means more resident time for heat and mass transfer, T_h –T_c becomes smaller and T_h decreases quickly, which leads to a much lower flux but a higher *PR*.

Resistance analysis to radial heat and mass transfer

The actual driving force in CEMD arises from temperature difference between T_{hp} and T_{af}, which is smaller than the bulk temperature difference between T_h and T_c. This phenomenon could be described using a temperature polarization coefficient (*TPC*), which is defined as

$$TPC = \frac{T_{hp} - T_{af}}{T_h - T_c} \tag{45}$$

Table 7 shows the summary of radial heat- and mass-transfer coefficients for both modules under the operating condition of T_3 = 80°C, T_1 = 35°C, and F = 32 L/h. From Table 7, it can be seen that h_h for Module 2 was larger than that for Module 1 owing to a thinner porous fiber used. h_c ranged from 6579.1–7012.9 W/m^2·°C, which was in accordance with the results studied by Song et al.[45] The mass-transfer resistance in the air gap ($1/K_a$) occupied the total mass-transfer resistance ($1/K_p$ + $1/K_a$) around 26.9% for Module 1 and around 35.5% for Module 2, respectively. Thus, compared with the air gap, the porous wall is the main resistance for mass transfer. Figure 14 shows the calculated

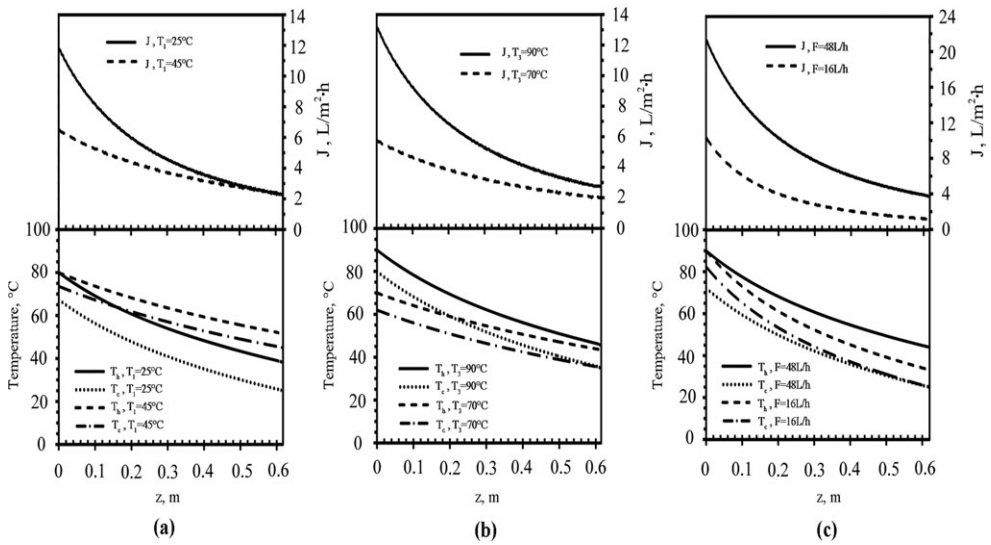

Figure 13. Axial temperature and flux profiles under different operation conditions: comparison (a) between T_1 = 25°C and T_1 = 45°C at T_3 = 80°C and F = 32 L/h; (b) between T_3 = 70°C and T_3 = 90°C at T_1 = 35°C and F = 32 L/h; (c) between F = 16 L/h and F = 48 L/h at T_1 = 25°C and T_3 = 90°C using Module 1.

Table 7. Comparison of Radial Heat and Mass Transfer Coefficients between Two Modules*

Region	Heat or mass transfer coefficients	Module 1	Module 2
Boundary layer of hot side	h_h, W/m^2·°C	4247.3–4466.4	7661.9–8120.8
Porous wall	$k_{pe}/r_{pi}ln(r_{po}/r_{pi})$, W/m^2·°C	414.36	728.25
	K_p, kg/m^2·Pa·s	$(2.934–3.761)\times10^{-7}$	$(3.615–4.777)\times10^{-7}$
Air gap	$k_a/\delta_a(r_{po}/r_{pi})$, W/m^2·°C	96.22	78.04
	K_a, kg/m^2·Pa·s	$(7.02–11.67)\times10^{-7}$	$(5.54–10.20)\times10^{-7}$
Distillate film	h_f, W/m^2·°C	13163–86229	13930–103620
Dense wall	$k_d/r_{di}ln(r_{do}/r_{di})$, W/m^2·°C	2703.5	2703.5
Boundary layer of cold side	h_c, W/m^2·°C	6579.1–6980.7	6578.6–7012.9

*Operating condition: $T_3 = 80$ °C, $T_1 = 35$ °C and $F = 32$L/h.

radial temperature profiles based on the theoretical model without heat loss at the first and last slice of both modules at the same aforementioned operating condition. The temperature change in the radial direction is indicative of heat-transfer resistance. Since the heat-transfer coefficient for the air gap is the lowest, the temperature drop in the air domain ($T_{pa} - T_{af}$) is the highest. $T_{fd} - T_{dc}$ was about 2.5-fold of $T_{dc} - T_c$ as shown in Figure 14, because the heat-transfer coefficient of the boundary layer of the cold side is about 2.5-fold of that of the dense wall, which indicates that the dense wall resistance is primarily controlling when nonporous PP hollow fibers are used as an internal heat exchanger for recovery of latent heat. As the amount of transported heat and mass is larger at the upper than that at the bottom, *TPC* at the first slice (0.57 and 0.63 for Module 1 and 2, respectively) is smaller than that at the last slice (0.83 and 0.89 for Module 1 and Module 2, respectively). h_f for the thickest condensed film at the last slice remains as high as around 10^4 W/m^2·°C, which only results in a temperature drop ($T_{af} - T_{fd}$) of at most 0.1°C. From Figure 14, to make *TPC* get close to 1.0, it is necessary to enhance h_h and h_c, such as by reducing the porous fiber diameter and the thickness of boundary layer, and meanwhile also to enhance the heat-transfer coefficient for the dense wall such as by increasing the thermal conductivity of materials or further reducing the dense wall thickness.

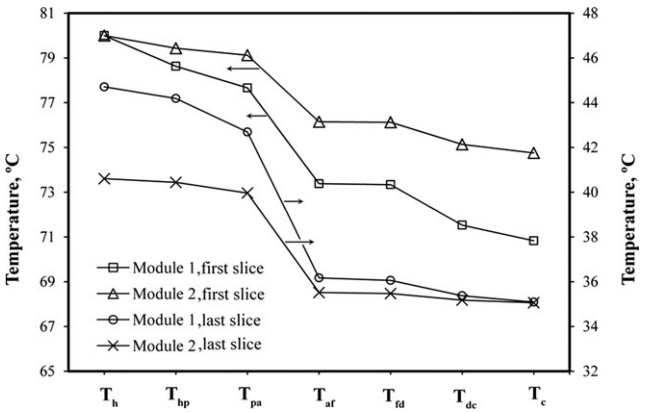

Figure 14. Radial temperature profiles at the first and last slice within both modules under the operating condition: $T_3 = 80$°C, $T_1 = 35$°C and $F = 32$ L/h.

Effect of module parameters on system performance

Module parameters mainly include the thickness of air gap (δ_a), the number ratio of porous fibers to dense-wall fibers (N_d/N_p), and the length of module (l). With the help of theoretical model, taking Module 2 under the constant operating condition of $T_3 = 90$°C, $T_1 = 45$°C and $F = 16$ L/h as an example, the effect of δ_a, N_d/N_p and l on flux is shown in Figure 15a–c and that on *PR* and η is shown in Figure 16a–c. When one parameter is changed, the other two parameters are

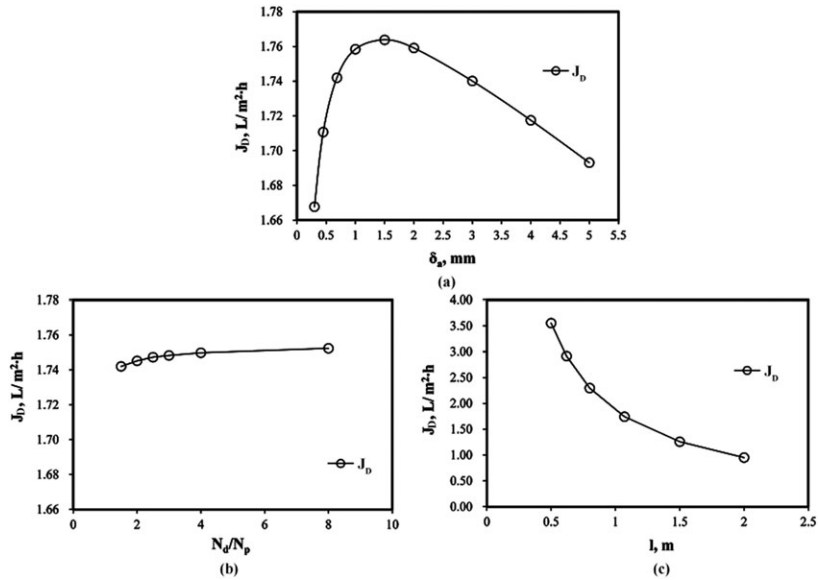

Figure 15. Effect of (a) δ_a, (b) N_d/N_p, and (c) l on J_D under the operating condition of $T_3 = 90$°C, $T_1 = 45$°C and $F = 16$ L/h using Module 2 by theoretical model.

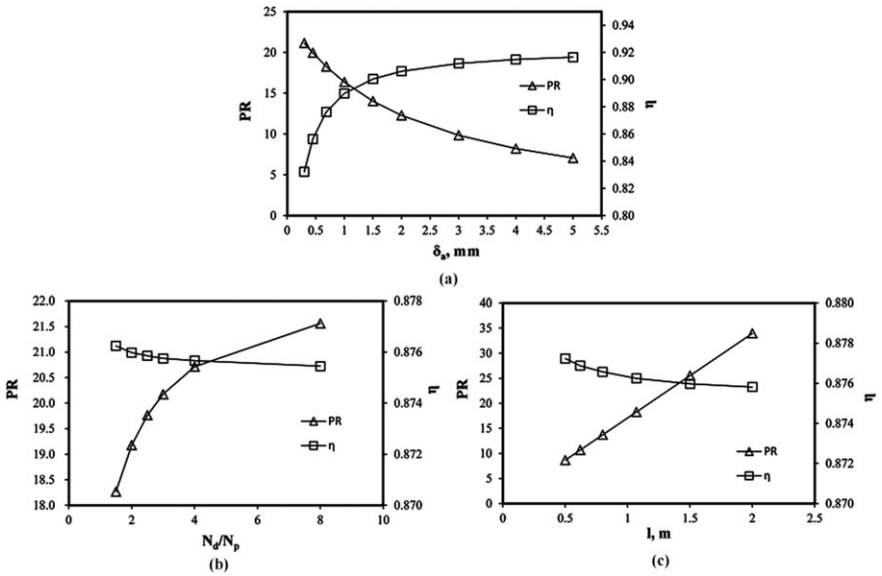

Figure 16. Effect of (a) δ_a, (b) N_d/N_p, and (c) l on PR and η under the operating condition of $T_3 = 90°C$, $T_1 = 45°C$ and $F = 16$ L/h using Module 2 by theoretical model.

kept constant as the original value shown in Table 1. There exists an optimal δ_a for J_D, around 1.5×10^{-3}m. Air gap is efficient in preventing heat conduction and keeping large radial temperature difference, thus, with the increase of δ_a, PR gradually decreases and η increases, but the mass-transfer resistance also increases. As mentioned previously, at original $\delta_a = 6.85 \times 10^{-4}$m, the air gap is not the main resistance for mass transfer, thus, a further increase of δ_a ($<1.5 \times 10^{-3}$m) will increase the flux. Increase of N_d/N_p from 1.5 to 8.0 has little effect on J_D and η, but PR increases by 18.0%. Large surface area for condensation is beneficial for heat recovery. The length of module has a strong effect on both J_D and PR. η slightly changes with l. Increase of l from original 1.07 m to the supposed 2.0 m will enhance the PR from 18.3 to 33.9, and the flux will decrease from 1.74 L/m^2·h to 1.17 L/m^2·h. According to Hagen-Poiseuille equation, the inlet pressure of the porous fibers will also increase about twofold of original one, so a proper length should be chosen to avoid membrane wetting. In a practical application, due to the complexity of the module configuration, especially for large-scale module fabrication, maldistribution of hollow fibers which leads to a large thickness of the air gap may result in bad performance. Thus, well controlled module parameters are vital for the system performance in the industrial scale.

Application of CEMD for concentrating the dilute sugar solution

As previously mentioned, flux-PR trade-off exists when choosing the proper operating conditions. Therefore, decision-making of process parameters should be fully considered in the real needs. Usually, the typical temperature for cellulase hydrolysis is around 50°C. Considering the required time for concentration, a proper flux is also necessary. Thus, Module 2 was used under the condition of $T_3 = 90°C$, $T_1 = 45°C$, and $F = 32$ L/h. The results of concentration, ΔT_{top}, J_D and PR evolution with time are given in Figure 17a–b. During the concentration, the distillate water was of good quality and no sugar was detected. It took nearly 6 h to obtain nearly 9.8 L of pure water, and the final concentration (143.3 g/L glucose and 70.3 g/L xylose) was around 12 times of the initial one, which could be efficiently fermented to ethanol with a suitable concentration for the following purification. It was observed that at the end of the concentration, ΔT_{top} was increased by about 0.5°C, and the flux was slightly decreased by 8.1% from 3.33 L/m^2·h to 3.06 L/m^2·h. PR was, thus, decreased by 10.9% from 9.20 to 8.20. The two inlet pressures were also increased by about 1.65-fold since the viscosity of feed increases with concentration.

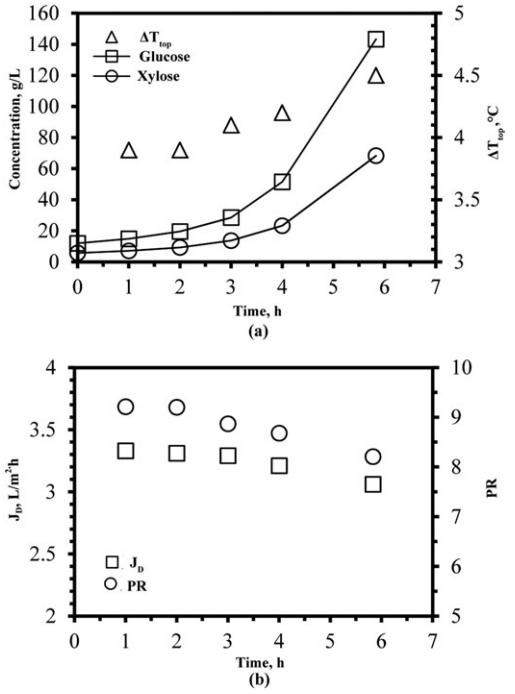

Figure 17. (a) Concentration and ΔT_{top}, and (b) flux and PR evolution with time during concentrating the dilute aqueous solution with initial concentration of 12 g/L glucose and 6 g/L xylose using Module 2 under $T_3 = 90°C$, $T_1 = 45°C$ and $F = 32$ L/h.

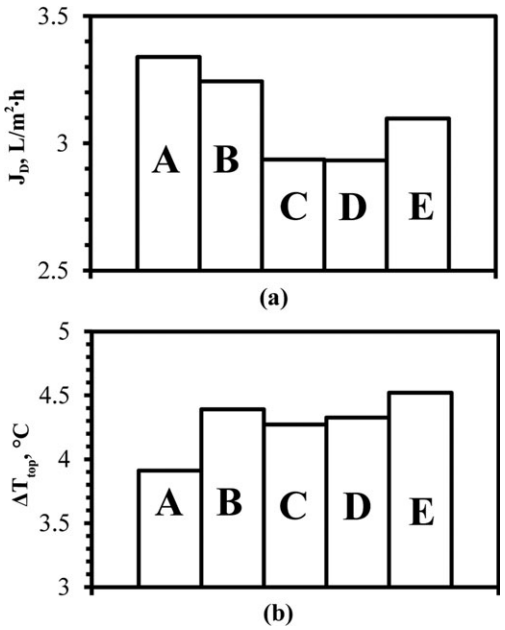

Figure 18. Effect of properties of final aqueous sugar solution compared with pure water on (a) flux, and (b) ΔT_{top} by theoretical model.

A: Pure water; B: Effect of water activity; C: Combined effect of water activity and heat capacity; D: Combined effect of water activity, heat capacity and thermal conductivity; E: Combined effect of water activity, heat capacity, thermal conductivity and density.

In hollow fiber-based membrane distillation for laminar flow, the effect of viscosity at a concentration below 40 wt % on heat-transfer coefficient in the lumen side of both fibers, and the concentration polarization could be neglected.[46] Decline of flux and *PR* during concentration would mainly attribute to the change of the physical properties of the feed such as water activity, heat capacity, thermal conductivity and density. Properties of final aqueous solution with a total sugar concentration of 211.6 g/L were estimated,[46,47] which was compared with that of pure water: heat capacity decreases from 4,200 J/kg·°C to 3,800 J/kg·°C; water activity declines from 1.000 to 0.975; thermal conductivity decreases by about 10%, and the density from 1.00 g/L increases to 1.06 g/L. Figure 18a and b shows the effect of these physical properties on the flux, and ΔT_{top} in light of the theoretical model. It can be found that a small reduction of water activity causes small flux decay, but increases ΔT_{top} greatly (comparison between A and B); reduction of heat capacity which leads to fast axial temperature drop greatly reduces flux and decreases ΔT_{top} slightly (comparison between B and C); decrease of thermal conductivity which would to some extent increase the thickness of the boundary layer has a limited effect on flux decay and an increase of ΔT_{top} (comparison between C and D); increase of density which leads to slow axial temperature drop enhances J_D and increases ΔT_{top}. Because of the decline of flux and the increase of ΔT_{top}, and also decrease of heat capacity, *PR* was predicted to decrease by about 11.3%, which reasonably explained the experimental data.

Concluding Remarks

A CEMD process based on hollow fiber AGMD module with internal latent-heat-recovery was successfully developed, and performance of two CEMD modules made from different commercial porous fibers was both experimentally and theoretically demonstrated. This article led to the following statements:

1 High value of *PR* and high selectivity were shown experimentally in the laboratory-scale of developed processes, which proves that CEMD process has its potential to be energetically competitive with other thermal or membrane processes for future application in the industrial scale.

2 The theoretical model in light of governing transport equations could be used to describe the effect of operating variables, module parameters and also physical properties of feed-in on process performance, such as flux, performance ratio and evaporation efficiency. The model accuracy was verified by the experimental observations.

3 Both RSM regression and theoretical modeling revealed that like other processes with heat recovery, there existed a tradeoff between flux and *PR*.

4 The theoretical model predicted possible ways to obtain a much higher *PR*, such as good insulation, high-operating temperature, selection of porous fiber with high mass-transfer coefficient, increase of module length, reduction of the thermal resistance of dense wall, and also the boundary thickness, and so on.

5 Dilute aqueous sugar solution was successfully concentrated about 12 times by using CEMD process. With the increase of sugar concentration, flux and *PR* decreased to some extent, but at the final stage, flux and PR (as high as 8.20 in this study) were still appreciated.

Acknowledgments

The authors are grateful to Dr. C.M. Guijt for the helpful suggestions.

Notation

$C_{p,v}$ = specific heat capacity of water vapor, 1876 J/kg·°C
d_p = average pore size of porous wall, μm
g = = 9.81 m/s^2
$k_a\ k_d\ k_p$ = thermal conductivity for the air filled in the pores, 0.28 W/m·°C, the solid polymeric matrix,0.17 W/m·°C, and the dense wall,0.12 W/m·°C
$K_a\ K_p$ = mass-transfer coefficient for air gap and porous wall, kg/m^2·Pa·s
M_w = water molecular weight, 0.018 kg/mol
$p_0\ p_w$ = total pressure, 101325 Pa and water vapor partial pressure, Pa
$p_{w,\delta}$ = water vapor partial pressure at the location of δ, Pa
$p_{w,pa}\ p_{w,af}$ = water vapor partial pressure at the interface between porous fiber and air gap, between air gap and distillate film, Pa
$Q_c\ Q_h$ = absorbed heat amount into the dense-wall fibers and released heat amount from the porous fibers at any location, J/h
r = distance from center of porous fiber, m
r' = distance from center of dense-wall fiber, m
$r_{di}\ r_{do}$ = inner and outside radius of dense-wall fiber, m
$r_{pi}\ r_{po}$ = inner and outside radius of of porous fiber, m
R = gas constant, 8.314 J/mol·°C
$T_c\ T_f\ T_h$ = temperature of cold feed, distillate film and hot feed at any location, °C
$T_{hp}\ T_{pa}\ T_{af}\ T_{fd}\ T_{dc}$ = temperature at the interface between hot flow and porous fiber, between porous fiber and air gap, between air gap and distillate film, and between distillate film and cold flow at any location, °C
$T_r\ T_\delta$ = temperature of water vapor at the location of r and δ, °C
$W_c\ W_f\ W_h$ = mass flow rate of cold feed, distillate film and hot feed at any location, kg/h

z = distance from the top of the module, m
β_0 γ_0 = intercept
β_i γ_i = linear coefficient
β_{ii} γ_{ii} = squared coefficient
β_{ij} γ_{ij} = interaction coefficient
δ = distance from the interface between the outside surface of porous fiber and the air gap, m
ε = porosity
τ = tortuosity factor for porous fiber

Literature Cited

1. Lawson KW, Lloyd DR. Membrane distillation. *J Membr Sci*. 1997;124:1–25.
2. Curcio E, Drioli E. Membrane distillation and related operations-a review. *Sep Purif Rev*. 2005;34:35–86.
3. El-Bourawi MS, Ding Z, Ma R, Khayet M. A Framework for better understanding membrane distillation separation process. *J Membr Sci*. 2006;285:4–29.
4. Ettouney HM, El-Dessouky HT, Faibish RS, Gowin PJ. Evaluating the economics of desalination. *Chem Eng Prog*. 2002;98:32–39.
5. Qtaishat M, Matsuura T, Kruczek B, Khayet M. Heat and mass transfer analysis in direct contact membrane distillation. *Desalination*. 2008;219:272–292.
6. Al-Obaidani S, Crucio E, Macedonio F, Di Profio G, Al-Hinai H, Drioli E. Potential of membrane distillation in seawater desalination: thermal efficiency, sensitivity study and cost estimation. *J Membr Sci*. 2008;323:85–98.
7. Li B, Sirkar KK. Novel membrane and device for direct contact membrane distillation-based desalination process. *Ind Eng Chem Res*. 2004;43:5300–5309.
8. Li B, Sirkar KK. Novel membrane and device for vacuum membrane distillation-based desalination process. *J Membr Sci*. 2005;257:60–75.
9. Banat FW, Simandl J. Desalination by membrane distillation: a parametric study. *Sep Sci Technol*. 1998;33:201–226.
10. Liu GL, Zhu C, Cheung CS, Leung CW. Theoretical and experimental studies on air gap membrane distillation. *Heat Mass Transfer*. 1998;34:329–335.
11. Alklaibi AM, Lior N. Comparative study of direct-contact and air-gap membrane distillation processes. *Ind Eng Chem Res*. 2007;46:584–590.
12. Cheng LH, Wu PC, Chen JH. Numerical simulation and optimal design of AGMD-based hollow fiber modules for desalination. *Ind Eng Chem Res*. 2009;48:4948–4959.
13. Hanbury WT, Hodgkiess T. Membrane distillation-an assessment. *Desalination*. 1985;56:287–297.
14. Shoji Kimura, Shin-ichi Nakao. Transport phenomena in membrane distillation. *J Membr Sci*. 1987;33:285–298.
15. Fane AG, Schfiled RW, Fell CJD. The efficient use of energy in membrane distillation. *Desalination*. 1987;64:231–243.
16. Kurokawa H, Sawa T. Heat recovery characteristics of membrane distillation. *Heat Transfer Jap Res*. 1996;25:135–150.
17. Gilron J, Song LM, Sirkar KK. Design for cascade of crossflow direct contact membrane distillation. *Ind Eng Chem Res*. 2007;46:2324–2334.
18. Lee HY, He F, Song LM, Gilron, Sirkar KK. Desalination with a cascade of cross-flow hollow fiber membrane distillation devices integrated with a heat exchanger. *AIChE J*. 2011;54:1780–1795.
19. Henderyckx Y, inventor. Evaporation-condensation recovery of a solution component using vapor-permeable wall spaced from a cold wall. US Patent 3,563,860. February 16, 1971.
20. Gore WL, Gore RW, Gore DW, inventors. WL Gore & Associates, Inc., assignee. Desalination device and process. US Patent 4,545,862. October 8, 1985.
21. Koschikowski J, Wieghaus M, Rommel M. Solar thermal-driven desalination plants based on membrane distillation. *Desalination*. 2003;156:295–304.
22. Guijt CM, Racz IG, Van Heuven JW, Reith T, de Haan AB. Modelling of a transmembrane evaporation module for desalination of seawater. *Desalination*. 1999;126:119–125.
23. Guijt CM, Meindersma GW, Reith T, de Haan AB. Air gap membrane distillation 2. Model validation and hollow fibre module performance analysis. *Sep Purif Technol*. 2005;43:245–255.
24. Hanemaaijer JH, Van Heuven JW, inventors; TNO, assignee. Method for the purification of a liquid by membrane distillation, in particular for the production of desalinated water from seawater or brackish water or process water. US Patent 6,716,355 B1. April 6, 2004.
25. Meindersmaa GW, Guijt CM, de Haan AB. Desalination and water recycling by air gap membrane distillation. *Desalination*. 2006;187:291–301.
26. Zacchi G, Axelsson A. Economic evaluation of preconcentration in production of ethanol from dilute sugar solutions. *Biotechnol Bioeng*. 1989;34:223–233.
27. Li DF, Wang R, Chung TS. Fabrication of lab-scale hollow fiber membrane modules with high packing density. *Sep Purif Technol*. 2004;40:15–30.
28. Majumdar S, Guha AK, Sirkar KK. A new liquid membrane technique for gas separation. *AIChE J*. 1988;34:1135–1145.
29. Sengupta A, Basu R, Sirkar KK. Separation of solutes from aqueous solutions by contained liquid membranes. *AIChE J*. 1988;34:1698–1708.
30. Basu R, Sirkar KK. Hollow fiber contained liquid membrane separation of citric acid. *AIChE J*. 1991;37:383–393.
31. Izquierdo-Gil MA, Garci'a-Payo MC, Fernández-Pineda C. Air gap membrane distillation of sucrose aqueous solutions. *J Membr Sci*. 1999;155:291–307.
32. Guijt CM. *Influence of Membrane Properties and Air Gap on the Performance of a Membrane Distillation Module* [Ph.D. Thesis]. University of Twente, Enschede, The Netherlands; 2003.
33. Guijt CM, Meindersma GW, Reith T, de Haan AB. Air gap membrane distillation 1. Modelling and mass transport properties for hollow fibre membranes. *Sep Purif Technol*. 2005;43:233–244.
34. Bird RB, Stewart WE, Lightfoot EN. *Transport Phenomena*. 2nd ed. New York: John Wiley & Sons, Inc.; 2002:446–448.
35. Alklaibi AM, Lior N. Transport analysis of air-gap membrane distillation. *J Membr Sci*. 2005;255:239–253.
36. Martínez-Díez L, Vázquez-Gonzàlez MI. Temperature polarization in mass transport through hydrophobic porous membranes. *AIChE J*. 1996;42:1844–1852.
37. Bandini S, Saavedra A, Sarti G C. Vacuum membrane distillation: Experiments and modeling. *AIChE J*. 1997;43:l398–408.
38. Khayet M, Cojocaru C, García-Payo C. Application of response surface methodology and experimental design in direct contact membrane distillation. *Ind Eng Chem Res*. 2007;46:5673–5685.
39. Chang H, Liau JS, Ho CD, Wang WH. Simulation of membrane distillation modules for desalination by developing user's model on Aspen Plus platform. *Desalination*. 2009;249:380–387.
40. Onsekizoglua P, Bahcecib KS, Acara J. The use of factorial design for modeling membrane distillation. *J Membr Sci*. 2010;349:225–230.
41. Qin YJ, Cabral J, Wang SC. Hollow-fiber gas-membrane process for removal of NH_3 from solution of NH_3 and CO_2. *AIChE J*. 1996;42:1945–1956.
42. Qin YJ, Cabral J. Lumen mass transfer in hollow-fiber membrane processes with constant external resistances. *AIChE J*. 1997;42:1975–1988.
43. Alves VD, Koroknai B, Bélafi-Bakó K, Coelhoso IM. Using membrane contactors for fruit juice concentration. *Desalination*. 2004;162:263–270.
44. Song LM, Li B, Sirkar KK, Gilron J. Direct contact membrane distillation-based desalination: novel membranes, devices, larger-scale studies, and a model. *Ind Eng Chem Res*. 2007;46:2307–2323.
45. Song LM, Li B, Zarkadas D, Christian S, Sirkar K K. Polymeric hollow-fiber heat exchangers for thermal desalination processes. *Ind Eng Chem Res*. 2010;49:11961–11977.
46. Laganà F, Barbieri G, Drioli E. Direct contact membrane distillation: modeling and concentration experiments. *J Membr Sci*. 2000;166:1–11.
47. Cerdeiriña CA, Carballo E, Tovar CA, Romaní L. Thermodynamic properties of aqueous carbohydrate solutions. *J Chem Eng Data*. 1997;42:124–127.

Manuscript received Feb. 23, 2012, and revision received July 12, 2012.